

Correlation Calibration: A Hybrid Calibration Technique for Radio Interferometric Arrays

ROBERT PASCUA ^{1,2,3} JONATHAN SIEVERS ¹ AND ADRIAN LIU ¹

¹*Department of Physics and Trotter Space Institute, McGill University
3600 University Street*

Montreal, QC H3A 2T8, Canada

²*Dunlap Institute for Astronomy and Astrophysics, University of Toronto
50 St. George Street*

Toronto, ON M5S 3H4, Canada

³*Perimeter Institute for Theoretical Physics*

31 Caroline Street North

Waterloo, ON N2L 2Y5, Canada

ABSTRACT

Calibrating out per-antenna signal chain effects is an essential step in analyzing radio interferometric data. For drift-scanning arrays, robustly calibrating the data is especially challenging due to the lack of the ability to track a calibration source. Consequently, calibration strategies for drift-scanning arrays are limited by our knowledge of the radio sky at large, as well as the direction-dependent instrument response. In the context of 21 cm cosmology, where small calibration errors can conspire to overwhelm the cosmological signal, it is therefore crucially important to develop calibration strategies that are capable of accurately calibrating the data in the presence of sky or instrument modeling errors. In this paper we present CorrCal, a covariance-based calibration strategy for redundant radio interferometric arrays. CorrCal is a hybrid calibration strategy that leverages the strengths of traditional sky-based calibration and redundant calibration in a computationally efficient framework that is fairly insensitive to modeling errors. We find that calibration errors from CorrCal are unbiased and far below typical thermal noise thresholds across a wide range of modeling error scenarios. We show that CorrCal is computationally efficient: our implementation is capable of evaluating the likelihood and its gradient in less than a second for 1,000-element class arrays using just a single laptop core. Given CorrCal's computational efficiency and robustness to modeling errors, we anticipate that it will serve as a useful tool in the analysis of radio interferometric data from current and next-generation experiments targeting the cosmological 21 cm signal.

1. INTRODUCTION

Calibration is a fundamental challenge in the analysis of radio interferometric data. Calibration takes the raw interferometric visibilities, which have been modulated by the electronics in the signal chain, and converts them into physically meaningful quantities by establishing an absolute flux scale and a common phase center, enabling downstream analyses such as mapmaking or power spectrum estimation. Traditional approaches to calibration tend to rely on the ability to steer the individual array elements, since it is fairly straightfor-

ward to establish an absolute flux scale and calibrate out the relative phases between antennas when the array is pointing at a bright, well-known source of radio emission that dominates the measured visibilities. Many current and next-generation arrays, however, have opted to instead take a drift-scan approach, where array elements are not steerable but instead observe different patches of sky in accordance with the Earth's rotation. Notably, experiments such as the Hydrogen Epoch of Reionization Array (HERA, DeBoer et al. 2017; Berkhout et al. 2024), the Canadian Hydrogen Intensity Mapping Experiment (CHIME, CHIME Collaboration et al. 2022), the Canadian Hydrogen Observatory and Radio-transient Detector (CHORD, Vanderlinde et al. 2020), and the Hydrogen Intensity and Real-time Analysis eX-

periment (HIRAX, Newburgh et al. 2016; Crichton et al. 2022) have adopted a drift-scan approach because it allows for a more economical array element design that can be produced at scale. With the increasing prevalence of drift-scanning arrays, there is an increasing need for innovative approaches to calibration—in the absence of a reliable calibration source, it is much more difficult to establish an absolute reference. These new drift-scanning arrays also tend to operate at low frequencies, where our knowledge of the sky and the instrument response are both highly uncertain. The need for improved calibration routines is accentuated in the context of 21 cm cosmology, where the extreme dynamic range between the cosmological signal and the astrophysical foreground signal (Liu & Shaw 2020) demands exquisite control over systematic effects in the data (e.g., Barry et al. 2016; Joseph et al. 2018; Byrne et al. 2019; Orosz et al. 2019). In this paper, we present Correlation Calibration, which we will hereafter refer to as *CorrCal*, a hybrid approach to calibration that simultaneously leverages the strengths of calibration routines often employed in drift-scanning arrays and significantly reduces the calibration errors induced by modeling errors.

While there exists a myriad of approaches to calibration (e.g., Yatawatta et al. 2009; Liu et al. 2010; Dillon et al. 2018; Byrne et al. 2021; Ewall-Wice et al. 2022; Sims et al. 2022a,b; Byrne 2023; Cox et al. 2024), the majority of direction-independent calibration algorithms tend to fall into one of two categories: sky-based calibration or redundant calibration. In sky-based calibration, the per-antenna direction-independent *gains* are obtained by modeling radio sources on the sky and the direction-dependent instrument response. The expected visibilities measured by the array are then computed from the sky model and instrument response and the per-antenna gains are adjusted to find the best-fit solution given the observed data. Naturally, sky-based calibration is prone to errors in modeling the radio sky as well as errors in modeling the instrument response. In redundant calibration, the expected visibilities are not computed from a sky and instrument model, but are instead treated as free parameters that are fit for in the calibration process (Liu et al. 2010; Dillon et al. 2018). This approach relies on regularity in the interferometric array, leveraging the fact that for an array of identical antennas, the measured visibilities are uniquely determined (up to instrumental noise) by the corresponding baselines. Since the physical separation between the antennas used to form a visibility uniquely determines the measured visibility (up to the antenna response), different pairs of antennas that form the same baseline will produce “redundant” measurements. Arrays with

elements placed on a regular grid will therefore generate several “redundant groups” of baselines, each of which produces multiple independent measurements of the same visibility. These repeated measurements allow the analyst to infer the expected visibilities from the data rather than explicitly model the expected visibilities prior to calibrating the data. In reality, the exact placement of antennas will deviate somewhat from their ideal positions in regular arrays, and there will be variations in the dish construction and feed placement from one antenna to another. It therefore follows that there will always be some degree of nonredundancy in real interferometric arrays, and this nonredundancy may propagate to errors in the calibration solutions (Orosz et al. 2019). Additionally, because redundant calibration only requires that the data are consistent within each redundant group, it can at best provide a relative calibration between elements in an array. Consequently, there are a few degeneracies in the calibration solutions that leave the absolute flux scale and phase center of the data entirely unconstrained. The degeneracies inherent to redundant calibration solutions require that an additional “absolute” calibration is applied following redundant calibration (Kern et al. 2020). Absolute calibration is typically carried out in a similar way to sky-based calibration, but modifications to the gains are restricted to the degenerate subspace of the redundant calibration solutions. Both sky-based calibration and redundant calibration are therefore subject to modeling errors, and the resulting calibration errors may be limiting systematics in the search for the cosmological 21 cm signal (Barry et al. 2016; Li et al. 2018).

In light of the increasingly urgent need for improved calibration techniques, there have been several recent efforts to improve on sky-based and redundant calibration (e.g., Byrne et al. 2021; Ewall-Wice et al. 2022; Sims et al. 2022a,b). Among the recent innovations in calibration, the unified calibration approach from Byrne et al. (2021) bears the closest resemblance to *CorrCal*. Their approach essentially utilizes a redundant calibration likelihood that is supplemented by a sky-based prior to jointly fit for the per-antenna gains and the model visibilities in a Bayesian framework. In other words, they enforce that the data are internally consistent while providing extra information about what they expect each unique baseline to measure. Byrne et al. (2021) demonstrate that their unified calibration scheme produces calibration solutions that are more accurate than those obtained through redundant calibration or sky-based calibration. An important omission from their work, however, is the scalability of their approach and therefore whether it is a *practical* tool for calibrating current and

next-generation interferometric data given the immense data rates from these instruments and the computational resources available for calibration.

CorrCal is a new calibration technique that simultaneously leverages the strengths of sky-based calibration and redundant calibration in a computationally efficient framework that is resilient to modeling errors. In this paper, we extend the work of Sievers (2017), which initially presented CorrCal. We provide a thorough derivation of the formalism underpinning CorrCal and detail how CorrCal achieves an efficient covariance-based approach to calibrating radio interferometric data. We improve on the original algorithm by properly normalizing the likelihood used to obtain the calibration solutions with very little additional computational overhead. This is an important advancement, since the calibration solutions from the previous implementation (which included only a simple regularization on the average gain phase) featured a curvature across the array due to not properly accounting for the number of redundant groups each antenna participated in. We build on the tests that were performed in Sievers (2017) by more systematically investigating how CorrCal responds to various modeling errors. These are end-to-end tests of CorrCal that simulate visibilities from a model of the sky and the instrument response, apply per-antenna gains and thermal noise, then use CorrCal to infer the gains that were applied to the simulated data. In our tests, we explore a broad range of ways in which our calibration model may be inaccurate to develop a thorough understanding of how CorrCal will perform in a variety of realistic scenarios. All of the results presented in this paper were obtained using a new implementation of CorrCal that is publicly available on GitHub¹ and contains extensive documentation, unit testing, and tutorials.

The remainder of the paper is organized in the following way. In Section 2, we present the formal foundation underlying CorrCal, setting the stage for Section 3 where we show how the baseline–baseline covariance takes on a sparse form and describe how the components in the sparse covariance may be modeled. In Section 4, we provide an overview of how CorrCal leverages the sparsity of the baseline–baseline covariance to attain an efficient covariance-based calibration. In Section 5, we present the results of a suite of validation tests designed to determine whether modeling errors manifest as calibration errors. In Section 6, we briefly summarize the results presented in this paper.

2. CORRELATION CALIBRATION

Calibration is fundamentally a problem of parameter estimation. We have a prior belief that the data may be described by a parametric model, which we use to construct a loss function that quantifies how well the model fits the data for a given set of model parameters. The parameters in our model provide us with a means for translating the raw data into the physically meaningful quantities measured by the telescope. Minimizing the loss function with respect to the calibration parameters therefore provides us with the best estimate of the physically meaningful data products, insofar as our model is an accurate description of the data.

Traditional approaches to calibration assume that differences between the data and the model are driven by Gaussian distributed thermal noise. Accordingly, the best-fit model can be obtained by minimizing a χ^2 statistic,

$$\chi^2 = \sum_k \frac{|d_k - m_k(\boldsymbol{\theta})|^2}{\sigma_k^2}, \quad (1)$$

where d_k are the measured data (i.e., the interferometric visibilities), $m_k(\boldsymbol{\theta})$ is the model of the data characterized by parameters $\boldsymbol{\theta}$, σ_k^2 is the variance in each measurement due to thermal noise, and k indexes over different data used in the fit. Said differently, traditional approaches to calibration rely on modeling the *expectation value* of the data and tweaking the model parameters to minimize the residuals in the fit given the noise level in the data. CorrCal, on the other hand, uses a model of the expected *covariance* in the data and tweaks the model parameters to obtain the best-fit to the measured covariance. Contrary to traditional approaches to calibration, where the covariance is typically immutable, CorrCal treats the covariance as a mutable object that is varied in the calibration algorithm. In the context of CorrCal, the covariance structure of the data is determined by the instrument response and the radio emission on the sky and we must therefore carefully consider how these terms manifest in the covariance between measured visibilities.

Formally, we treat the data as a vector of mean-zero, correlated Gaussian random variables and maximize the likelihood that the measured data are drawn from the distribution characterized by our model covariance. We model the data as a mixture of three independent Gaussian components: one term characterizes thermal noise in the visibilities; one term characterizes covariances that arise from the presence of bright, unresolved emission on the sky (i.e., point sources); and the last characterizes the visibility–visibility covariance associated with diffuse emission in the form of a correlated Gaussian

¹ <https://github.com/r-pascua/corrcal>

random field. Because CorrCal takes a radically different approach to modeling the data when compared to traditional calibration strategies, the (implicitly or explicitly) assumed symmetry in the covariance of the residuals between the data and the model of the data is broken in the context of CorrCal. The symmetry breaking is most apparent in the case of a single point source at the array’s phase center, which results in purely real-valued visibilities. In the context of CorrCal, this case is modeled as data whose variance is contained entirely within its real component—with each realization of the observed source brightness, the imaginary part of the data will remain zero while the real part will fluctuate. More broadly speaking, a point source will typically generate unequal variance in the real and imaginary parts of the data and a nonzero covariance between the real and imaginary parts, which motivates the need to treat the real and imaginary parts of the data as separate random variables with some nontrivial covariance. Formally, the presence of point sources breaks circular symmetry in the statistics of the residuals between the data and the model of the data, which requires one to treat either the real and imaginary parts of the data as separate random variables or the visibility and its complex conjugate as separate random variables. In other words, because of how we choose to model the data, a single complex-valued covariance matrix provides insufficient information for completely characterizing the statistical distribution of the data.

Of the two options presented in the previous paragraph, we opt to treat the real and imaginary parts of the data as separate random variables. We accordingly arrange the data into a purely real-valued vector that alternates between the real and imaginary components, so that

$$\mathbf{d}^T = \left(d_1^R, d_1^I, d_2^R, d_2^I, \dots, d_N^R, d_N^I \right), \quad (2)$$

where d_k^R indicates the real part of the k -th visibility, d_k^I indicates the imaginary part, and N is the number of baselines used for calibration.² The data covariance $\mathbf{d}\mathbf{d}^T$ then consists of 2×2 blocks,

$$\mathbf{d}\mathbf{d}^T = \begin{pmatrix} d_1^R d_1^R & d_1^R d_1^I & \cdots & d_1^R d_N^R & d_1^R d_N^I \\ d_1^I d_1^R & d_1^I d_1^I & \cdots & d_1^I d_N^R & d_1^I d_N^I \\ \vdots & \vdots & \ddots & \vdots & \vdots \\ d_N^R d_1^R & d_N^R d_1^I & \cdots & d_N^R d_N^R & d_N^R d_N^I \\ d_N^I d_1^R & d_N^I d_1^I & \cdots & d_N^I d_N^R & d_N^I d_N^I \end{pmatrix}, \quad (3)$$

² In this paper, we restrict our attention to a per-frequency, per-time implementation of CorrCal, so that k only indexes different baselines.

where each 2×2 block provides the covariance between the real and imaginary parts of the visibilities for the corresponding pair of baselines.

Since we are treating the data as mean-zero, correlated Gaussian random variables, we use a multivariate Gaussian probability density as our likelihood,

$$\mathcal{L} \propto (\det \mathbf{C})^{-1/2} \exp\left(-\frac{1}{2} \mathbf{d}^T \mathbf{C}^{-1} \mathbf{d}\right), \quad (4)$$

where \mathbf{C} is our model of the baseline–baseline covariance, which we describe in detail in the following section. The model covariance contains our calibration parameters, so we obtain a calibration solution by minimizing the negative log-likelihood

$$-\log \mathcal{L} = \log \det \mathbf{C} + \mathbf{d}^T \mathbf{C}^{-1} \mathbf{d}, \quad (5)$$

where we have discarded any constant terms and overall scalings since these do not affect the location of the minimum. The log-determinant term provides a normalization on the calibration parameters which, when taken together with the generalized χ^2 term $\mathbf{d}^T \mathbf{C}^{-1} \mathbf{d} = \text{tr}(\mathbf{d}\mathbf{d}^T \mathbf{C}^{-1})$, where $\text{tr}(\dots)$ is the trace operator, ensures that the best-fit solution produces the model covariance that is the closest match to the data covariance.

To more clearly see why our choice of likelihood ensures that CorrCal optimally matches the model covariance \mathbf{C} to the data covariance $\mathbf{d}\mathbf{d}^T$, consider the derivative of the negative log-likelihood with respect to the covariance matrix elements,

$$-\frac{\partial \log \mathcal{L}}{\partial C_{ij}} = \frac{1}{\det \mathbf{C}} \frac{\partial \det \mathbf{C}}{\partial C_{ij}} + \mathbf{d}^T \frac{\partial \mathbf{C}^{-1}}{\partial C_{ij}} \mathbf{d}. \quad (6)$$

The derivative of the determinant is given by Jacobi’s formula, so that

$$\frac{\partial \det \mathbf{C}}{\partial C_{ij}} = \det \mathbf{C} (\mathbf{C}^{-1})_{ij}. \quad (7)$$

Since the derivative of the inverse can be rewritten via

$$\frac{\partial \mathbf{C}^{-1}}{\partial C_{ij}} = -\mathbf{C}^{-1} \frac{\partial \mathbf{C}}{\partial C_{ij}} \mathbf{C}^{-1}, \quad (8)$$

we can rewrite the derivative of the generalized χ^2 term as

$$\mathbf{d}^T \frac{\partial \mathbf{C}^{-1}}{\partial C_{ij}} \mathbf{d} = -\sum_{m,n} d_m (\mathbf{C}^{-1})_{mi} (\mathbf{C}^{-1})_{jn} d_n. \quad (9)$$

This result, taken together with Jacobi’s formula, allows us to express the derivative of the negative log-likelihood with respect to the covariance as

$$-\frac{\partial \log \mathcal{L}}{\partial \mathbf{C}} = \mathbf{C}^{-1} - \mathbf{C}^{-1} \mathbf{d}\mathbf{d}^T \mathbf{C}^{-1}, \quad (10)$$

and therefore the negative log-likelihood is minimized when $\mathbf{C} = \mathbf{d}\mathbf{d}^T$. While this is formally not an admissible solution, because this best-fit covariance is not invertible (since $\mathbf{C} = \mathbf{d}\mathbf{d}^T$ is rank 1), the result carries a useful conceptual interpretation. By choosing to maximize the likelihood in Equation 4, we are therefore mathematically encoding our decision to perform calibration by fitting a model of correlations between visibilities to the observed correlations in the data. Furthermore, the normalization term is crucial for ensuring that the likelihood is maximized when the model covariance matches the data covariance—a different choice of normalization would result in a different optimal covariance.

The calculation provided in the previous paragraph suggests that the optimal solution for our covariance-based approach is to make the covariance model exactly match the observed data covariance. In the context of calibrating radio interferometric data, however, we are instead solving a *constrained* optimization problem: we are combining covariance optimization with the assumptions of radio interferometry. When we perform calibration we are not fitting the model covariance matrix elements directly, but rather each matrix element is a function of the calibration parameters. While this is partially due to the fact that fitting the individual matrix elements is an extremely under-constrained problem, our main motivation is that the covariance matrix elements on their own do not provide us with a link between the raw data and the physically meaningful telescope outputs. In the next part of this section, we derive a physically-motivated model of the covariance between visibilities that simultaneously leverages array redundancy and sky-based information.

2.1. Correlating Visibilities

We begin the calculation of the model covariance \mathbf{C} with the model m_k for the visibilities,

$$m_k = G_k \int A_k(\hat{\mathbf{r}}) I(\hat{\mathbf{r}}) e^{-i2\pi\nu \mathbf{b}_k \cdot \hat{\mathbf{r}}/c} d\Omega + n_k, \quad (11)$$

where k indexes over baselines, $A_k(\hat{\mathbf{r}})$ is the primary beam for baseline k in direction $\hat{\mathbf{r}}$, $I(\hat{\mathbf{r}})$ is the intensity of radio emission on the sky, $\mathbf{b}_k = \mathbf{x}_{k_2} - \mathbf{x}_{k_1}$ (where \mathbf{x}_i is the position of antenna i) is the spatial separation between antennas k_1 and k_2 , ν is the observed frequency, c is the speed of light in vacuum, $d\Omega$ is the differential solid angle element, $G_k \equiv g_{k_1} g_{k_2}^*$ is the k -th entry of the “gain matrix”, g_{k_1} and g_{k_2} are the direction-independent gains, and n_k is radiometer noise. If we arrange the model visibilities into a purely real-valued vector \mathbf{m} so that

$$\mathbf{m}^T = (m_1^R, m_1^I, \dots, m_N^R, m_N^I), \quad (12)$$

then the model covariance \mathbf{C} is computed via

$$\mathbf{C} = \langle \mathbf{m}\mathbf{m}^T \rangle, \quad (13)$$

where $\langle \dots \rangle$ indicates an ensemble average. Just like the data covariance $\mathbf{d}\mathbf{d}^T$, the model covariance consists of 2×2 blocks,

$$\mathbf{C} = \begin{pmatrix} \mathbf{C}_{11} & \cdots & \mathbf{C}_{1N} \\ \vdots & \ddots & \vdots \\ \mathbf{C}_{N1} & \cdots & \mathbf{C}_{NN} \end{pmatrix}, \quad (14)$$

with each 2×2 block \mathbf{C}_{ij} taking the form

$$\mathbf{C}_{ij} = \begin{pmatrix} \langle m_i^R m_j^R \rangle & \langle m_i^R m_j^I \rangle \\ \langle m_i^I m_j^R \rangle & \langle m_i^I m_j^I \rangle \end{pmatrix}. \quad (15)$$

We model the sky intensity $I(\hat{\mathbf{r}})$ as a mean-zero Gaussian random field, which we decompose into a diffuse component and a point source component via

$$I(\hat{\mathbf{r}}) = \mathcal{D}(\hat{\mathbf{r}}) + \sum_j s_j \delta^D(\hat{\mathbf{r}} - \hat{\mathbf{r}}_j), \quad (16)$$

where $\delta^D(\dots)$ is the Dirac delta. We assume that the diffuse component $\mathcal{D}(\hat{\mathbf{r}})$ is uncorrelated with each source, and that the flux density s_j from a source is uncorrelated with that of any other source. In other words, we treat the sky as a mixture of mutually independent Gaussian random components, which is equivalent to treating the data as a sum of mutually independent Gaussian random variables. The sky covariance is therefore

$$\begin{aligned} \langle I(\hat{\mathbf{r}}) I(\hat{\mathbf{r}}') \rangle &= \langle \mathcal{D}(\hat{\mathbf{r}}) \mathcal{D}(\hat{\mathbf{r}}') \rangle \\ &+ \sum_j S_j^2 \delta^D(\hat{\mathbf{r}} - \hat{\mathbf{r}}_j) \delta^D(\hat{\mathbf{r}}' - \hat{\mathbf{r}}_j), \end{aligned} \quad (17)$$

where S_j^2 is the variance in the flux density for source j . Qualitatively, this model of the sky covariance relies on our ability to characterize the power spectrum of the diffuse emission and our ability to localize a handful of bright point sources and roughly characterize their brightness.

While our formalism assumes that the sky is a mean-zero Gaussian random field, we know that in reality the radio sky has a much richer statistical description. The discrepancy between the true sky and our assumed model of the sky is not, however, a limiting factor in Corrcal’s ability to obtain accurate and precise calibration solutions, as we show in Section 5.3. The key to understanding why lies in the fact that we are choosing to optimize the covariance rather than the expectation value, and in doing so we are explicitly choosing

to ignore moments of the foreground distribution beyond the power spectrum. By approximating the diffuse emission as a Gaussian random field, we are essentially choosing to leverage the Gaussian component of the foreground signal, which we think we know reasonably well and which should provide sufficient information for calibrating the data. In fact, redundant calibration implicitly makes essentially the same assumption about the sky (as we show by recovering redundant calibration as a limiting case of CorrCal in [Appendix A](#)), albeit without any assumption about the observed foreground power spectrum. With the demonstrated success of redundant calibration (e.g., [Dillon et al. 2020](#); [HERA Collaboration et al. 2022](#)), there should be little concern that non-Gaussianity in the sky signal would hinder CorrCal’s ability to accurately calibrate the data. Moreover, any non-Gaussian features in the foreground distribution will be imprinted in phase correlations, which is precisely the type of information captured by the point source covariance term and ignored by the diffuse covariance term. Because the diffuse covariance ignores phase correlations in the foregrounds by construction, any known non-Gaussianities in the diffuse foreground signal would need to be captured through modifications to the point source covariance. It therefore follows that ignoring non-Gaussian features in the diffuse foreground signal is tantamount to excluding point sources from the point source covariance model, which we show in [Section 5.4](#) merely acts to modify the phase gradient in the best-fit gain solution.

3. MODELING THE DATA COVARIANCE

Our model of covariances in the data consists of three terms that we assume are statistically independent of one another: a term associated with diffuse emission on the sky, a term associated with point source emission on the sky, and a term associated with radiometer noise. Since these three components are mutually independent, the model covariance also consists of three terms and may be written as

$$\mathbf{C} = \mathbf{N} + \mathbf{D} + \mathbf{S}, \quad (18)$$

where \mathbf{N} characterizes the thermal noise variance, \mathbf{D} characterizes the covariance associated with the diffuse component, and \mathbf{S} characterizes the covariance associated with point source emission. The noise term is straightforward to compute, since radiometer noise is circularly symmetric and Gaussian, and uncorrelated

between visibilities.³ If the noise variance in the visibilities is σ_k^2 for the k -th baseline, then the noise matrix is diagonal with entries

$$\text{diag}(\mathbf{N}) = \frac{1}{2} \left(\sigma_1^2, \sigma_1^2, \dots, \sigma_N^2, \sigma_N^2 \right), \quad (19)$$

since half of the variance is in the real part and the other half is in the imaginary part. The other two terms in the covariance require more work to compute, which we will cover in the following two sections.

3.1. Point Source Covariance

Since we are modeling the point source contributions as Dirac delta terms in [Equation 16](#), the integral in our model visibility ([Equation 11](#)) is transformed into a sum over sources, so that

$$m_k^{\text{source}} = G_k \sum_j s_j A_k(\hat{\mathbf{r}}_j) e^{-i2\pi\nu\mathbf{b}_k \cdot \hat{\mathbf{r}}_j/c}. \quad (20)$$

We may rewrite this in terms of a *beam transfer function* $B_k(\hat{\mathbf{r}}) \equiv A_k(\hat{\mathbf{r}}) \exp(-i2\pi\mathbf{u}_k \cdot \hat{\mathbf{r}})$ as

$$m_k^{\text{source}} = G_k \sum_j s_j B_k(\hat{\mathbf{r}}_j). \quad (21)$$

The real and imaginary parts of the model visibility may thus be written as a sum over matrix-vector products via

$$\begin{pmatrix} m_k^{\text{source},R} \\ m_k^{\text{source},I} \end{pmatrix} = \sum_j s_j \begin{pmatrix} G_k^R & -G_k^I \\ G_k^I & G_k^R \end{pmatrix} \begin{pmatrix} B_k(\hat{\mathbf{r}}_j)^R \\ B_k(\hat{\mathbf{r}}_j)^I \end{pmatrix}, \quad (22)$$

where again the R, I superscripts indicate the real and imaginary parts, respectively. This may be written more compactly in matrix notation as

$$\mathbf{m}_k^{\text{source}} = \sum_j s_j \mathbf{G}_k \mathbf{B}_k(\hat{\mathbf{r}}_j), \quad (23)$$

where the various terms are defined as

$$\mathbf{m}_k^{\text{source}} = \begin{pmatrix} m_k^{\text{source},R} \\ m_k^{\text{source},I} \end{pmatrix}, \quad (24a)$$

$$\mathbf{B}_k(\hat{\mathbf{r}}) = \begin{pmatrix} B_k(\hat{\mathbf{r}})^R \\ B_k(\hat{\mathbf{r}})^I \end{pmatrix}, \quad (24b)$$

$$\mathbf{G}_k = \begin{pmatrix} G_k^R & -G_k^I \\ G_k^I & G_k^R \end{pmatrix}. \quad (24c)$$

³ There are cases where the noise *is* correlated between visibilities, such as when a very bright source dominates the total system temperature; however, this would be absorbed as an overall amplitude error in the source covariance and therefore is not an issue.

Using this more compact notation, the covariance between baseline \mathbf{b}_k and baseline $\mathbf{b}_{k'}$ due to the presence of point sources on the sky can be written as

$$\begin{aligned} \mathbf{S}_{kk'} &\equiv \left\langle \mathbf{m}_k^{\text{source}} \mathbf{m}_{k'}^{\text{source},T} \right\rangle \\ &= \sum_j S_j^2 \mathbf{G}_k \mathbf{B}_k(\hat{\mathbf{r}}_j) \mathbf{B}_{k'}(\hat{\mathbf{r}}_j)^T \mathbf{G}_{k'}^T. \end{aligned} \quad (25)$$

We may further simplify this by defining the *source matrix* $\mathbf{\Sigma}$ such that

$$\mathbf{\Sigma} = \begin{pmatrix} S_1 B_1(\hat{\mathbf{r}}_1)^R & \cdots & S_M B_1(\hat{\mathbf{r}}_M)^R \\ S_1 B_1(\hat{\mathbf{r}}_1)^I & \cdots & S_M B_1(\hat{\mathbf{r}}_M)^I \\ \vdots & \ddots & \vdots \\ S_1 B_N(\hat{\mathbf{r}}_1)^R & \cdots & S_M B_N(\hat{\mathbf{r}}_M)^R \\ S_1 B_N(\hat{\mathbf{r}}_1)^I & \cdots & S_M B_N(\hat{\mathbf{r}}_M)^I \end{pmatrix}, \quad (26)$$

where M is the number of sources included in the covariance model. In terms of the source matrix $\mathbf{\Sigma}$ and the gain matrix \mathbf{G} , the source covariance \mathbf{S} can be written as

$$\mathbf{S} = \mathbf{G} \mathbf{\Sigma} \mathbf{\Sigma}^T \mathbf{G}^T, \quad (27)$$

where the gain matrix \mathbf{G} is block-diagonal with 2×2 blocks along the diagonal given by Equation 24c. Evidently, the source covariance is *sparse* in the sense that the full $2N \times 2N$ baseline-baseline covariance is completely characterized by the $2N \times M$ source matrix, along with the block-diagonal gain matrix which contains the pairwise products of the per-antenna gains. In the following section, we will show that the diffuse covariance is also sparse, and in Section 4 we will show how the sparsity of the model covariance may be leveraged to efficiently apply CorrCal to large interferometric arrays.

3.2. Diffuse Covariance

We may simplify the covariance of the diffuse sky component by either expanding the diffuse term in spherical harmonics via

$$\mathcal{D}(\hat{\mathbf{r}}) = \sum_{\ell,m} a_{\ell m} Y_{\ell}^m(\hat{\mathbf{r}}), \quad (28)$$

where $Y_{\ell}^m(\hat{\mathbf{r}})$ are the spherical harmonics normalized so that $\int Y_{\ell}^m(\hat{\mathbf{r}}) Y_{\ell'}^{m'}(\hat{\mathbf{r}}) d\Omega = \delta_{\ell\ell'} \delta_{mm'}$, or by taking the flat-sky limit of Equation 11 and Fourier transforming the diffuse component from the image plane to the uv -plane via

$$\mathcal{D}(\theta_x, \theta_y) = \int \tilde{\mathcal{D}}(u, v) e^{i2\pi(u\theta_x + v\theta_y)} dudv. \quad (29)$$

Under the assumption that the diffuse component is a correlated, statistically isotropic Gaussian random field,

the spherical harmonic coefficients $a_{\ell m}$ obey the relation

$$\langle a_{\ell m} a_{\ell' m'}^* \rangle = C_{\ell} \delta_{\ell\ell'} \delta_{mm'}, \quad (30)$$

where C_{ℓ} is the angular power spectrum of the diffuse emission and δ_{ij} is the Kronecker delta. The analogous relation for the uv -modes $\tilde{\mathcal{D}}(u, v)$ is given by

$$\langle \tilde{\mathcal{D}}(\mathbf{u}) \tilde{\mathcal{D}}(\mathbf{u}')^* \rangle = P(|\mathbf{u}|) \delta^D(\mathbf{u} - \mathbf{u}'), \quad (31)$$

where $\mathbf{u}^T = (u, v)$, and $P(|\mathbf{u}|)$ is the flat-sky power spectrum of the diffuse emission. We may use the relations from Equation 30 and Equation 31 to express the covariance for the diffuse component in two ways via

$$\langle \mathcal{D}(\hat{\mathbf{r}}) \mathcal{D}(\hat{\mathbf{r}}') \rangle = \sum_{\ell,m} C_{\ell} Y_{\ell}^m(\hat{\mathbf{r}}) Y_{\ell}^m(\hat{\mathbf{r}})^*, \quad (32)$$

$$\langle \mathcal{D}(\boldsymbol{\theta}) \mathcal{D}(\boldsymbol{\theta}') \rangle = \int P(|\mathbf{u}|) e^{i2\pi \mathbf{u} \cdot (\boldsymbol{\theta} - \boldsymbol{\theta}')} dudv, \quad (33)$$

where $\boldsymbol{\theta}^T = (\theta_x, \theta_y)$. In the remainder of this section, we will use the latter expression to derive the form of the baseline-baseline covariance associated with diffuse emission, as it provides a more straightforward and intuitive calculation.

Rather than directly compute the real and imaginary terms in the diffuse covariance, we will instead compute the complex-valued covariance \mathbf{K} and pseudo-covariance $\mathbf{\Gamma}$ and construct the diffuse covariance from these terms. We first define the complex-valued diffuse model visibility as

$$\mathbf{v}^T = \left(m_1^{\text{diffuse}}, m_2^{\text{diffuse}}, \dots, m_N^{\text{diffuse}} \right), \quad (34)$$

where the individual m_k^{diffuse} are obtained from Equation 11 using $I(\hat{\mathbf{r}}) = \mathcal{D}(\hat{\mathbf{r}})$. With this definition, the complex-valued covariance is given by $\mathbf{K} \equiv \langle \mathbf{v} \mathbf{v}^{\dagger} \rangle$ and the pseudo-covariance is given by $\mathbf{\Gamma} \equiv \langle \mathbf{v} \mathbf{v}^T \rangle$. In terms of the complex-valued covariance \mathbf{K} and pseudo-covariance $\mathbf{\Gamma}$, the diffuse model covariance \mathbf{D} may be computed via

$$2\mathbf{D}^{RR} = \text{Re}(\mathbf{K} + \mathbf{\Gamma}), \quad (35a)$$

$$2\mathbf{D}^{II} = \text{Re}(\mathbf{K} - \mathbf{\Gamma}), \quad (35b)$$

$$2\mathbf{D}^{RI} = -\text{Im}(\mathbf{K} - \mathbf{\Gamma}), \quad (35c)$$

$$2\mathbf{D}^{IR} = \text{Im}(\mathbf{K} + \mathbf{\Gamma}), \quad (35d)$$

where the R, I superscripts indicate the covariance between the real and imaginary components, respectively. Expressed as integrals in the uv -plane, the matrix elements of the complex-valued covariance and pseudo-covariance may be written as

$$K_{kk'} = G_k G_{k'}^* \int P(|\mathbf{u}|) \left[\int A_k(\boldsymbol{\theta}) e^{-i2\pi(\mathbf{u}_k - \mathbf{u}) \cdot \boldsymbol{\theta}} d\boldsymbol{\theta} \right] \left[\int A_{k'}(\boldsymbol{\theta}') e^{-i2\pi(\mathbf{u}_{k'} - \mathbf{u}) \cdot \boldsymbol{\theta}'} d\boldsymbol{\theta}' \right]^* d\mathbf{u}, \quad (36)$$

$$\Gamma_{kk'} = G_k G_{k'} \int P(|\mathbf{u}|) \left[\int A_k(\boldsymbol{\theta}) e^{-i2\pi(\mathbf{u}_k - \mathbf{u}) \cdot \boldsymbol{\theta}} d\boldsymbol{\theta} \right] \left[\int A_{k'}(\boldsymbol{\theta}') e^{-i2\pi(\mathbf{u}_{k'} + \mathbf{u}) \cdot \boldsymbol{\theta}'} d\boldsymbol{\theta}' \right] d\mathbf{u}, \quad (37)$$

where \mathbf{u}_k is the projection of the baseline onto the image plane (i.e., the tangent plane to the sky at boresight), measured in units of wavelengths. The terms in the square brackets are just the phase-shifted Fourier transforms of the beam, so we may simplify these expressions as

$$K_{kk'} = G_k G_{k'}^* \int P(|\mathbf{u}|) \tilde{A}_k(\mathbf{u}_k - \mathbf{u}) \tilde{A}_{k'}(\mathbf{u}_{k'} - \mathbf{u})^* d\mathbf{u}, \quad (38)$$

$$\Gamma_{kk'} = G_k G_{k'} \int P(|\mathbf{u}|) \tilde{A}_k(\mathbf{u}_k - \mathbf{u}) \tilde{A}_{k'}(\mathbf{u}_{k'} + \mathbf{u}) d\mathbf{u}, \quad (39)$$

where $\tilde{A}_k(\mathbf{u}_k - \mathbf{u})$ is the *beam kernel* shifted to the \mathbf{u} -mode sampled by baseline \mathbf{b}_k and reflected across the origin in the uv -plane. Note that if we restrict our attention to real-valued beams, then the beam kernel is Hermitian and therefore obeys $\tilde{A}_k(\mathbf{u}_k - \mathbf{u}) = \tilde{A}_k(\mathbf{u} - \mathbf{u}_k)^*$.

The diffuse covariance calculation may be simplified through physical arguments about the relation between the voltage beam $\mathbf{E}_a(\boldsymbol{\theta})$ for antenna a and the primary beam $A_k(\boldsymbol{\theta})$ for baseline k . In the absence of spillover effects, the voltage beam $\mathbf{E}_a(\boldsymbol{\theta})$ for a reflector antenna is obtained by taking the Fourier transform of the dish illumination pattern, which has compact support. The primary beam is the product of the antenna voltage beams,

$$A_k(\boldsymbol{\theta}) = \mathbf{E}_{k_1}(\boldsymbol{\theta}) \cdot \mathbf{E}_{k_2}(\boldsymbol{\theta})^*, \quad (40)$$

so according to the convolution theorem, the beam kernel $\tilde{A}_k(\mathbf{u})$ is the convolution of the Fourier transforms of the voltage beams. Since the Fourier transform of the voltage beam is the dish illumination pattern, it follows that the beam kernel must have compact support—the convolution of two compact functions is itself compact. This means that the beam kernel terms appearing in Equation 38 and Equation 39 have a hard edge in the uv -plane, and therefore only pairs of baselines with overlapping beam kernels will have a nonzero covariance. In addition, for any pair of sufficiently long baselines with a nonzero covariance, the pseudo-covariance must

be zero.⁴ Under an appropriate choice of conjugation convention for the antenna ordering in each baseline, such as requiring $v_k \geq 0$ for every baseline, every pair of baselines has zero pseudo-covariance, which allows us to simplify the diffuse covariance calculation as

$$\mathbf{D}^{RR} = \mathbf{D}^{II} = \frac{1}{2} \text{Re}(\mathbf{K}), \quad (41a)$$

$$\mathbf{D}^{RI} = -\mathbf{D}^{IR} = -\frac{1}{2} \text{Im}(\mathbf{K}). \quad (41b)$$

Figure 1 provides a schematic example of the overlap term $A_k(\mathbf{u}_k - \mathbf{u}) A_{k'}(\mathbf{u}_{k'} - \mathbf{u})^*$ for three pairs of baselines: one pair consists of two non-redundant baselines; another consists of two partially redundant baselines; and the third consists of perfectly redundant baselines. At a high level, Figure 1 provides us with a generalized view of redundancy: the redundancy between a pair of baselines may be measured by computing the overlap of their beam kernels in the uv -plane. Since the diffuse covariance is an integral of the beam overlap weighted by the sky power spectrum, Figure 1 provides us with a guide for understanding how different pairs of baselines contribute to the diffuse covariance. For the pair of non-redundant baselines, the overlap term is zero everywhere and the pair of baselines does not contribute to the diffuse covariance. For the pair of partially redundant baselines, there is a small region in the uv -plane where the product does not vanish, and therefore this pair would contribute somewhat to the diffuse covariance. For the pair of baselines that are perfectly redundant, the overlap term is nonzero for the largest possible region of the uv -plane for the provided primary beam, so these pairs of baselines dominate the structure of the diffuse covariance. Since the diffuse covariance terms are primarily dictated by the redundancy between each pair of baselines, the diffuse covariance acts as an analog to redundant calibration. In fact, as we show in Ap-

⁴ For some baselines that are roughly the length of the dish diameter, it is possible for both $\tilde{A}_k(\mathbf{u} - \mathbf{u}_k) \tilde{A}_{k'}(\mathbf{u} - \mathbf{u}_{k'})^*$ and $\tilde{A}_k(\mathbf{u} - \mathbf{u}_k) \tilde{A}_{k'}(\mathbf{u} + \mathbf{u}_{k'})$ to have nonvanishing regions of support (Myers et al. 2003). In these cases, both contributions must be included in the diffuse covariance calculation.

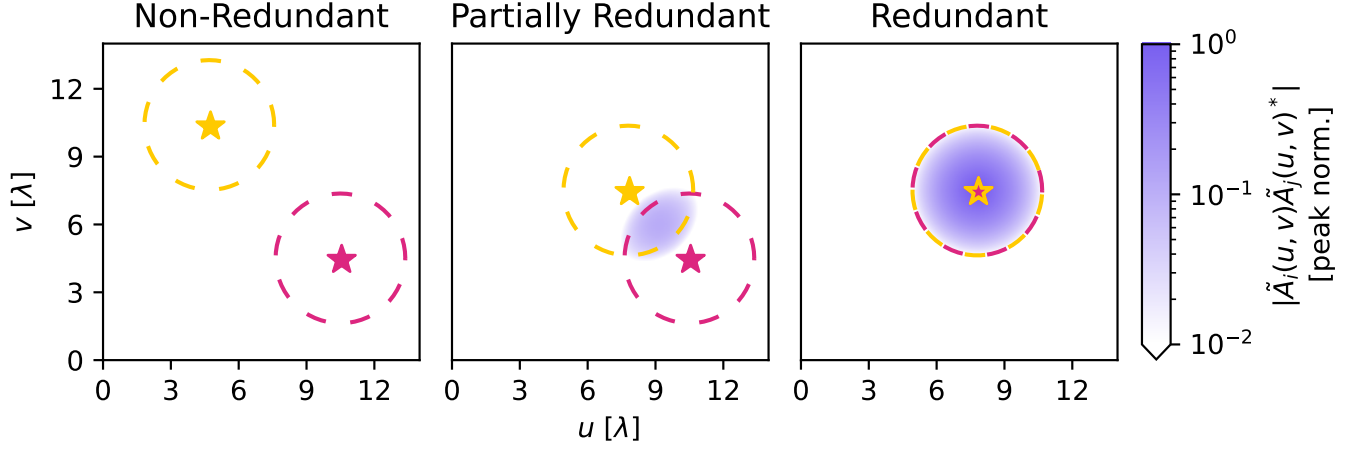


Figure 1. Schematic showing the product of the beam kernels in the overlap integral that is used to compute the diffuse covariance matrix elements. The dashed lines show the expected position of the first null in the beam kernel, the stars indicate the central uv modes sampled by the different baselines, and the color scale indicates the absolute value of the peak-normalized product of beam kernels at each point in the uv -plane. The left panel shows a pair of baselines that are considered non-redundant; the center panel shows a pair of baselines that are partially redundant; and the right panel shows a pair of baselines that are perfectly redundant.

pendix A, redundant calibration may be recovered from CorrCal under an appropriate set of analysis decisions.

These observations, combined with considerations about the array layout, may serve as a guide for how to construct the diffuse covariance. For a fully accurate description of the covariance, the contributions from both partially redundant and highly redundant baseline pairs should be included in the diffuse covariance. For a highly redundant array, however, it is reasonable to approximate the diffuse covariance structure by only computing terms for highly redundant baselines, and we show in Section 5 that good calibration solutions may be obtained when ignoring partial redundancy. For this work, we limit our focus to arrays without sub-aperture samplings and a modest buffer between adjacent antennas so that the complex-valued covariance is only nonzero for pairs of baselines within a redundant group—this is not a necessary restriction, but it allows for a substantial reduction in computational complexity at the cost of ignoring correlations between baselines that are only partially redundant.

Since we are ignoring correlations between partially redundant baselines when computing the diffuse covariance matrix elements, the diffuse covariance becomes block-diagonal when we sort the baselines into redundant groups. If we sort the baselines into R redundant

groups, then the diffuse covariance takes the form

$$\mathbf{D} = \begin{pmatrix} \mathbf{D}_1 & \mathbf{0} & \cdots & \mathbf{0} \\ \mathbf{0} & \mathbf{D}_2 & \ddots & \vdots \\ \vdots & \ddots & \ddots & \mathbf{0} \\ \mathbf{0} & \cdots & \mathbf{0} & \mathbf{D}_R \end{pmatrix}, \quad (42)$$

where \mathbf{D}_r is the baseline-baseline covariance for all baselines within redundant group r (i.e., all baselines with $|\mathbf{b}_k - \mathbf{b}_r| < \epsilon$ for some non-redundancy tolerance ϵ , where \mathbf{b}_r is the average baseline in redundant group r). For each redundant block \mathbf{D}_r we can perform an eigendecomposition via

$$\mathbf{D}_r = \mathbf{Q}_r \mathbf{\Lambda}_r^{1/2} \mathbf{\Lambda}_r^{1/2} \mathbf{Q}_r^{-1}, \quad (43)$$

where the columns of the matrix \mathbf{Q}_r are the eigenvectors for the redundant block \mathbf{D}_r and $\mathbf{\Lambda}_r$ is a diagonal matrix containing the corresponding eigenvalues. Since the redundant blocks \mathbf{D}_r are symmetric, real-valued matrices, the eigenvector matrices \mathbf{Q}_r are orthogonal and we may therefore write the eigendecomposition as

$$\mathbf{D}_r = \mathbf{Q}_r \mathbf{\Lambda}_r^{1/2} \mathbf{\Lambda}_r^{1/2} \mathbf{Q}_r^T. \quad (44)$$

If we define the block-diagonal *diffuse matrix* $\mathbf{\Delta}$ as

$$\mathbf{\Delta} = \text{diag}(\mathbf{Q}_1 \mathbf{\Lambda}_1^{1/2}, \cdots, \mathbf{Q}_R \mathbf{\Lambda}_R^{1/2}), \quad (45)$$

then the diffuse covariance is just $\mathbf{D} = \mathbf{G} \mathbf{\Delta} \mathbf{\Delta}^T \mathbf{G}^T$. As stated in the previous section, the diffuse covariance is a sparse matrix that may be characterized with just a

few eigenmodes per redundant group. If we only keep $2L$ eigenmodes per redundant block, then the $2N \times 2N$ terms in the diffuse covariance \mathbf{D} may be compressed into $2N \times 2L$ terms. Taken together with the results of the previous section, we conclude that the full baseline-baseline covariance has the following sparse representation:

$$\mathbf{C} = \mathbf{N} + \mathbf{G}\mathbf{\Delta}\mathbf{\Delta}^T\mathbf{G}^T + \mathbf{G}\mathbf{\Sigma}\mathbf{\Sigma}^T\mathbf{G}^T. \quad (46)$$

Rather than work with the dense covariance matrix, we may perform the operations in Equation 5 using the individual matrices \mathbf{N} , $\mathbf{\Delta}$, $\mathbf{\Sigma}$, and \mathbf{G} to efficiently perform calibration, as we will describe in greater detail in Section 4.

3.3. Calibrating with Correlations

Recall that the model covariance is determined by four matrices: the noise matrix, \mathbf{N} , which characterizes thermal fluctuations in the visibilities; the diffuse matrix, $\mathbf{\Delta}$, which encodes the array redundancy; the source matrix, $\mathbf{\Sigma}$, which establishes a reference to known point sources on the sky; and the gain matrix, \mathbf{G} , which contains the per-antenna complex gain factors. The simplest application of CorrCal requires the analyst to model the noise, diffuse, and source matrices, and leaves the per-antenna gains as free parameters that are solved for by minimizing the negative log-likelihood given by Equation 5. More sophisticated applications of CorrCal may add additional free parameters, such as per-antenna beam variations or feed positioning and pointing errors, but we defer these advanced applications to future work. In the remainder of this section, we provide a practical overview of applying CorrCal in the minimal calibration scenario.⁵

Determining the variance due to thermal fluctuations is relatively straightforward, with several viable options (see e.g., Tan et al. 2021 for a discussion of various methods for estimating thermal noise variance). The simplest estimate of the thermal noise variance may be obtained through the radiometer equation,

$$\sigma_k^2 = \frac{V_{k_1 k_1} V_{k_2 k_2}}{\delta\nu\delta t}, \quad (47)$$

where V_{aa} is the autocorrelation visibility for antenna a , k_1 and k_2 indicate the first and second antennas used to form the baseline \mathbf{b}_k , $\delta\nu$ is the bandwidth of a single frequency channel, and δt is the integration time. Alternatively, a more data-driven approach could estimate the variance through an appropriately weighted “inter-

leaved average” of the visibilities via

$$\sigma_k^2(\nu, t) = \frac{\left| \sum_{i=-n}^n \sum_{j=-m}^m w_{ij} V_k(\nu + i\delta\nu, t + j\delta t) \right|^2}{\sum_{i=-n}^n \sum_{j=-m}^m w_{ij}^2}. \quad (48)$$

If the weights w_{ij} are chosen such that the sum across any row or column vanishes, and the range of times and frequencies is kept small enough so that the signal approximately cancels (i.e., $V_k(\nu + i\delta\nu, t + j\delta t) \approx V_k(\nu, t)$), then this provides an unbiased estimate of the thermal noise variance at any observed frequency and time. Since the thermal noise variance may be estimated directly from the data, there is relatively very little work to be done by the analyst in constructing \mathbf{N} .

Constructing the source matrix (i.e., computing the matrix elements in Equation 26) is a bit more involved, but it is fairly straightforward to implement the results from Section 3.1. We may treat the source matrix $\mathbf{\Sigma}$ as a collection of source vectors \mathbf{s}_j so that

$$\mathbf{\Sigma} = \begin{pmatrix} \mathbf{s}_1 & \mathbf{s}_2 & \cdots & \mathbf{s}_M \end{pmatrix}, \quad (49)$$

where each source vector is given by

$$\mathbf{s}_j^T = S_j \left(B_1(\hat{\mathbf{r}}_j)^R, B_1(\hat{\mathbf{r}}_j)^I, \dots, B_N(\hat{\mathbf{r}}_j)^R, B_N(\hat{\mathbf{r}}_j)^I \right). \quad (50)$$

Each source vector \mathbf{s}_j may therefore be thought of as the contribution to the visibilities from the j -th source. In principle, one may include as many sources as desired in the source matrix; however, as more sources are included, the computational cost of evaluating the likelihood grows. In addition to the increase in computational cost, including more sources does not necessarily come with substantial improvements in calibration quality, as we will show in Section 5. We therefore recommend that a relatively small number of sources (ideally $M \ll N$, where N is the number of baselines used in calibration) are used to construct the source model, and that these M sources are chosen to account for the majority of the observed flux. A simple recipe based on this recommendation is as follows: First, use a model of the primary beam $A(\hat{\mathbf{r}})$, the observatory location, and a catalog of point source fluxes and positions to determine the observed flux for each source in the catalog; Next, choose the M sources with the greatest observed flux to serve as calibration sources; Next, evaluate the fringe $\exp(-i2\pi\nu\mathbf{b}_k \cdot \hat{\mathbf{r}}_j/c)$ for each baseline and each source; Finally, multiply the fringe terms by the corresponding observed fluxes and populate the source matrix accordingly. The resulting source matrix contains the expected contribution to the visibilities from each of the M brightest observed point sources for each baseline. The salient idea behind this approach is that the

⁵ For hands-on experience, please refer to the Calibration Tutorial notebook on the CorrCal GitHub repository.

brightest sources should provide the most stringent constraints on the phase correlations between the measured visibilities, and these sources would therefore provide the best calibration of the gain phases.

The diffuse matrix Δ calculation is more challenging to implement, but it is again fairly straightforward conceptually. Recall that each block of the diffuse covariance (Equation 42) describes correlations between visibilities within a redundant group and that the diffuse matrix contains the eigendecomposition of each block in the diffuse covariance (Equation 45). Conceptually, then, all we need to do is proceed block-by-block, computing the diffuse covariance according to Equation 38 and Equation 41 and assigning its eigendecomposition to the corresponding block in the diffuse matrix. The difficulty in implementation lies in how one chooses to evaluate the overlap integral in Equation 38, since some implementations are much more computationally expensive than other implementations. To simplify the calculation of the overlap integral, we first rewrite the diffuse sky power spectrum $P(|\mathbf{u}|)$ in terms of band powers p_α via

$$P(|\mathbf{u}|) = \sum_{\alpha} p_{\alpha} \mathcal{H}_{\alpha}(|\mathbf{u}|), \quad (51)$$

where

$$\mathcal{H}_{\alpha}(|\mathbf{u}|) = \begin{cases} 1, & \left| |\mathbf{u}| - |\mathbf{u}_{\alpha}| \right| \leq \epsilon \\ 0, & \text{else} \end{cases}, \quad (52)$$

for some $\epsilon > 0$. Expressing the power spectrum in this way may be thought of as binning the power spectrum into $|\mathbf{u}|$ -bins of equal width 2ϵ . Ignoring the gain factors in Equation 38, the diffuse covariance elements become

$$K_{kk'} = \delta_{r_k r_{k'}} p_{\alpha_r} \int_{|\mathbf{u}_{\alpha_r}| - \epsilon}^{|\mathbf{u}_{\alpha_r}| + \epsilon} \tilde{A}_k(\mathbf{u}_k - \mathbf{u}) \tilde{A}_{k'}(\mathbf{u}_{k'} - \mathbf{u})^* d\mathbf{u}, \quad (53)$$

where α_r is the bin containing the redundant baseline for group r , $\mathbf{u}_r \equiv N_{k \in r}^{-1} \sum_{k \in r} \mathbf{u}_k$ is the representative baseline for redundant group r , $N_{k \in r}$ is the number of baselines in group r , r_k indicates which redundant group contains baseline k , and $\delta_{r_k r_{k'}}$ encodes the block-diagonal structure of the diffuse covariance. Since the beam kernel $\tilde{A}_k(\mathbf{u}_k - \mathbf{u})$ is essentially nonzero only within some small region around \mathbf{u}_k , the overlap integral is effectively taken over a disk of radius ϵ centered on \mathbf{u}_{α_r} , so we may perform a change of variable to rewrite the integral as

$$K_{kk'} = \delta_{r_k r_{k'}} p_{\alpha_r} \int_{|\mathbf{u}| \leq \epsilon} \tilde{A}_k(\mathbf{u} - \delta \mathbf{u}_{k_r}) \tilde{A}_{k'}(\mathbf{u} - \delta \mathbf{u}_{k'_r})^* d\mathbf{u}, \quad (54)$$

where $\delta \mathbf{u}_{kr} \equiv \mathbf{u}_{\alpha_r} - \mathbf{u}_k$. Before simplifying the overlap integral any further, we will discuss the physical inter-

pretation of this result to help motivate further approximations.

In the limit that the data are perfectly redundant (i.e., $\delta \mathbf{u}_{kr} = 0$), the diffuse covariance elements converge to $K_{kk'} \rightarrow p_{\alpha_r} \Omega_{pp}$, where Ω_{pp} is the “beam-squared area”,

$$\Omega_{pp} \equiv \int |A(\hat{\mathbf{r}})|^2 d\Omega. \quad (55)$$

This is to be expected based on interferometric and statistical principles. Since an interferometer is most sensitive to fluctuations on the sky with an angular frequency of $\mathbf{u} = \mathbf{b}/\lambda$, it follows that the variance in the visibility should be proportional to the power spectrum of the sky emission at that same angular frequency. Since the measured visibility can be thought of as a weighted average of the sky intensity, where the weights are the beam transfer function $B(\hat{\mathbf{r}})$, the variance in the visibility will just be the variance of the sky multiplied by the sum of the square of the weights, which is Ω_{pp} . In the limit that the data are perfectly redundant, the covariance in any redundant block reduces to the variance in the redundant visibility multiplied by a matrix of ones, which is precisely what we computed above. When we relax the assumption of perfect redundancy, we should therefore expect that the redundant blocks scale with the amplitude of the power spectrum at the \mathbf{u} probed by each redundant group, with small excursions related to how the beams differ and how the baselines are mismatched. The diffuse covariance therefore performs two crucial roles in calibrating the data: first, the diffuse covariance establishes an approximate absolute flux scale⁶ by appealing to our expectation of the measured band-powers p_{α_r} ; second, the diffuse covariance provides a method of explicitly encoding our knowledge of array redundancy, thereby serving as a redundant calibration analog that allows for deviations from perfect redundancy.

While Equation 54 provides an intuitive expression for the diffuse covariance matrix elements, a direct evaluation of the overlap integral for every pair of baselines quickly becomes computationally expensive. The overlap integral may be considerably simplified by again appealing to the compact support of the beam kernel, which allows us to approximate the integral as a convolution over the entire uv -plane rather than a disk of radius ϵ . The convolution theorem allows us to rewrite

⁶ Importantly, the absolute flux scale established by CorrCal should typically not be taken at face value because the measured power may deviate from the expected power.

the overlap integral as a Fourier transform, which yields,

$$K_{kk'} \approx \delta_{r_k r_{k'}} p_{\alpha_r} \int A_k(\mathbf{l}) A_{k'}(\mathbf{l})^* e^{-i2\pi(\mathbf{u}_k - \mathbf{u}_{k'}) \cdot \mathbf{l}} d\mathbf{l}. \quad (56)$$

If we then assume that the non-redundancy is primarily sourced from antenna positioning errors, so that $A_k(\hat{\mathbf{r}}) = A(\hat{\mathbf{r}})$, and return to a curved sky integral, we get

$$K_{kk'} \approx \delta_{r_k r_{k'}} p_{\alpha_r} \int |A(\hat{\mathbf{r}})|^2 e^{-i2\pi(\mathbf{u}_k - \mathbf{u}_{k'}) \cdot \hat{\mathbf{r}}} d\Omega. \quad (57)$$

We may then expand the beam-squared term in spherical harmonics via

$$|A(\hat{\mathbf{r}})|^2 = \sum_{\ell, m} B_{\ell m} Y_{\ell}^m(\hat{\mathbf{r}}), \quad (58)$$

and use the spherical harmonic expansion of a plane wave,

$$e^{-i\mathbf{k} \cdot \mathbf{r}} = 4\pi \sum_{\ell, m} i^{\ell} j_{\ell}(kr) Y_{\ell}^m(\hat{\mathbf{k}}) Y_{\ell}^m(\hat{\mathbf{r}})^*, \quad (59)$$

where $k = |\mathbf{k}|$, $\hat{\mathbf{k}} = \mathbf{k}/k$, and j_{ℓ} is the spherical Bessel function of the first kind of order ℓ . These spherical harmonic expansions allow us to rewrite the integral as a sum over multipoles,

$$K_{kk'} \approx 4\pi \delta_{r_k r_{k'}} p_{\alpha_r} \sum_{\ell, m} B_{\ell m} i^{\ell} j_{\ell}(2\pi|\delta\mathbf{u}_{kk'}|) Y_{\ell}^m \left(\frac{\delta\mathbf{u}_{kk'}}{|\delta\mathbf{u}_{kk'}|} \right), \quad (60)$$

where $\delta\mathbf{u}_{kk'} \equiv \mathbf{u}_k - \mathbf{u}_{k'}$. Since the Bessel functions tend to decay rapidly with ℓ for typical values of $|\delta\mathbf{u}_{kk'}|$, it is usually sufficient to truncate this sum at $\ell \sim 10$ and obtain accurate estimates of the diffuse covariance elements. While this approximate form for the diffuse covariance elements required the assumption that all of the beams are identical, it still has practical applications since antenna-to-antenna beam variations are typically not known *a priori*. Naturally, however, an extension of CorrCal that fits for beam variations will need to rely on a different approach for computing the diffuse covariance elements.

4. IMPLEMENTATION

Thus far we have established that the guiding principle behind CorrCal is to fit a model of correlations between visibilities to the correlations observed in the data. As a covariance-based calibration technique, it is reasonable to assume that CorrCal would be computationally inefficient for large arrays—inverting an $N \times N$ matrix scales as $\mathcal{O}(N^3)$, and for a baseline–baseline covariance N scales with the square of the number of antennas in

the array. Recall, however, that by choosing to treat the sky as a Gaussian random field plus a collection of point sources, the baseline–baseline covariance matrix has a sparse representation. In this section, we show how the sparsity of the model covariance may be leveraged to enable a computationally efficient covariance-based calibration of interferometric arrays with a large number of antennas.

4.1. Sparse Two-Level Covariance

The core functionality of CorrCal revolves around the notion of a “sparse two-level” covariance, which alludes to the fact that both the covariance and some of its constituent matrices are sparse. Recall from Equation 46 that the baseline–baseline covariance \mathbf{C} is fully characterized by four matrices: \mathbf{N} , \mathbf{G} , $\mathbf{\Sigma}$, and $\mathbf{\Delta}$. Of these four matrices, only the source matrix $\mathbf{\Sigma}$ is not sparse. Since the noise matrix \mathbf{N} is diagonal (Equation 19) and the gain matrix \mathbf{G} is block-diagonal with each block a 2×2 matrix (Equation 24c), calculations involving these matrices are straightforward to implement efficiently. While the diffuse matrix $\mathbf{\Delta}$ is also block-diagonal (Equation 45) for the use case investigated in this paper, the inhomogeneous structure of the blocks requires additional care when implementing sparse matrix operations involving the diffuse matrix. In a more general context, the diffuse matrix may have off-diagonal terms, but these additional terms should be few in number because only a select few pairs of different baseline groups will have some degree of partial redundancy. A more general case that accounts for these additional correlations from partial redundancy will therefore also have a sparse representation, although a more sophisticated algorithm will be required to leverage the sparsity.

4.2. CorrCal Algorithm

Since the negative log-likelihood we employ to obtain calibration solutions is non-linear in the calibration parameters, we must employ an iterative optimization scheme to obtain the best-fit calibration solution. We opt to use a conjugate-gradient solver for finding the best-fit calibration solution, so it is imperative that we develop an efficient algorithm for computing the negative log-likelihood and its gradient. While the addition of the diagonal of the likelihood’s Hessian provides an order-of-magnitude reduction in the number of iterations required for convergence, there are numerical challenges with efficiently computing these terms that have yet to be resolved. Since the current application without the Hessian provides sufficiently accurate and expeditious calibration solutions, we defer the inclusion of the Hessian to future work. In the remainder of this

section, we describe the algorithm we use for computing the negative log-likelihood and its gradient. We close out the section with a brief discussion of the computational complexity of this implementation of CorrCal.

4.2.1. Likelihood Calculation

To perform calibration, we minimize the negative log-likelihood given in Equation 5. Since there is an overall phase degeneracy in the gain solutions, we augment Equation 5 with an additional Gaussian normalization on the average gain phase so that our objective function is

$$-\log \mathcal{L} = \log \det \mathbf{C} + \mathbf{d}^T \mathbf{C}^{-1} \mathbf{d} + \frac{|\sum_a \phi_a|^2}{N_{\text{ant}}^2 \sigma_{\text{phs}}^2}, \quad (61)$$

where $\phi_a = \arg(g_a)$ is the phase of antenna a , N_{ant} is the number of antennas, and σ_{phs}^2 is a parameter we may tune to change how strongly this prior is enforced. Since the number of baselines scales with the square of the number of antennas, the model covariance \mathbf{C} quickly becomes so large that it is computationally prohibitive to work with its dense representation. Fortunately, it is possible to work with individual matrices that appear in the sparse representation of the covariance in Equation 46—we never need to work with the $N_{\text{bl}} \times N_{\text{bl}}$ dense covariance.

The key to making the log-determinant and matrix inverse calculations in Equation 61 efficient stems from realizing that for a sparse covariance

$$\mathbf{C} = \mathbf{N} + \mathbf{\Delta} \mathbf{\Delta}^T + \mathbf{\Sigma} \mathbf{\Sigma}^T, \quad (62)$$

the inverse covariance also has a sparse representation,

$$\mathbf{C}^{-1} = \mathbf{N}^{-1} - \bar{\mathbf{\Delta}} \bar{\mathbf{\Delta}}^T - \bar{\mathbf{\Sigma}} \bar{\mathbf{\Sigma}}^T, \quad (63)$$

and the log-determinant can be easily accumulated while computing the “inverse” diffuse and source matrices $\bar{\mathbf{\Delta}}$ and $\bar{\mathbf{\Sigma}}$. We stress that the $\bar{\mathbf{\Delta}}$ and $\bar{\mathbf{\Sigma}}$ matrices are *not* the inverses of the diffuse and source matrices. We simply refer to $\bar{\mathbf{\Delta}}$ and $\bar{\mathbf{\Sigma}}$ as the “inverse” diffuse and source matrices because they perform a similar functional role in the sparse representation of the inverse covariance.

The inversion and log-determinant calculation is made computationally efficient by employing repeated applications of the Woodbury identity,

$$(\mathbf{A} + \mathbf{U} \mathbf{V}^T)^{-1} = \mathbf{A}^{-1} - \mathbf{A}^{-1} \mathbf{U} (\mathbf{I} + \mathbf{V}^T \mathbf{A}^{-1} \mathbf{U})^{-1} \mathbf{V}^T \mathbf{A}^{-1}, \quad (64)$$

alongside the Matrix Determinant Lemma,

$$\det(\mathbf{A} + \mathbf{U} \mathbf{V}^T) = \det(\mathbf{A}) \det(\mathbf{I} + \mathbf{V}^T \mathbf{A}^{-1} \mathbf{U}), \quad (65)$$

where in both expressions \mathbf{I} is the identity matrix. If required, the covariance may be obtained from the inverse

covariance by applying the “inverse” of the Woodbury identity,

$$(\mathbf{A} - \mathbf{U} \mathbf{V}^T)^{-1} = \mathbf{A}^{-1} + \mathbf{A}^{-1} \mathbf{U} (\mathbf{I} - \mathbf{V}^T \mathbf{A}^{-1} \mathbf{U})^{-1} \mathbf{V}^T \mathbf{A}^{-1}. \quad (66)$$

Applying the Woodbury identity to Equation 62, we obtain for the “inverse” diffuse matrix

$$\bar{\mathbf{\Delta}} = \mathbf{N}^{-1} \mathbf{\Delta} \mathbf{L}_{\Delta}^{-1T}, \quad (67)$$

where \mathbf{L}_{Δ} is obtained through a Cholesky factorization via

$$\mathbf{I} + \mathbf{\Delta}^T \mathbf{N}^{-1} \mathbf{\Delta} = \mathbf{L}_{\Delta} \mathbf{L}_{\Delta}^T. \quad (68)$$

For the “inverse” source matrix $\bar{\mathbf{\Sigma}}$ we find

$$\bar{\mathbf{\Sigma}} = (\mathbf{N}^{-1} - \bar{\mathbf{\Delta}} \bar{\mathbf{\Delta}}^T) \mathbf{\Sigma} \mathbf{L}_{\Sigma}^{-1T}, \quad (69)$$

where \mathbf{L}_{Σ} is defined via

$$\mathbf{I} + \mathbf{\Sigma}^T (\mathbf{N}^{-1} - \bar{\mathbf{\Delta}} \bar{\mathbf{\Delta}}^T) \mathbf{\Sigma} = \mathbf{L}_{\Sigma} \mathbf{L}_{\Sigma}^T. \quad (70)$$

The Cholesky factorizations in Equation 68 and Equation 70 contribute negligibly to the total computational cost, since they scale with the cube of the number of eigenmodes and the number of sources, respectively (both of which are small relative to the number of baselines). Using the Matrix Determinant Lemma, we can easily obtain the log-determinant via

$$\log \det \mathbf{C} = \log \det \mathbf{N} + 2 \log \det \mathbf{L}_{\Delta} + 2 \log \det \mathbf{L}_{\Sigma}. \quad (71)$$

Since the noise matrix \mathbf{N} is independent of the gains, we omit the $\log \det \mathbf{N}$ term when computing the log-determinant.

4.2.2. Gradient Calculation

We additionally provide an analytic calculation of the gradient of the negative log-likelihood (Equation 61) with respect to the real and imaginary components of the per-antenna gains,

$$-\partial \log \mathcal{L} = \text{Tr}(\mathbf{C}^{-1} \partial \mathbf{C}) + \mathbf{d}^T \partial \mathbf{C}^{-1} \mathbf{d} - \partial \log \mathcal{L}_{\phi}, \quad (72)$$

where $-\log \mathcal{L}_{\phi}$ is the phase normalization term. The gradient of the inverse covariance can be written in terms of the gradient of the covariance via

$$\partial \mathbf{C}^{-1} = -\mathbf{C}^{-1} \partial \mathbf{C} \mathbf{C}^{-1}, \quad (73)$$

so computing the gradient of the negative log-likelihood ultimately comes down to computing the gradient of the covariance and the gradient of the phase normalization term. Applying the product rule, the gradient of the covariance consists of four terms,

$$\begin{aligned} \partial \mathbf{C} &= \partial \mathbf{G} \mathbf{\Delta} \mathbf{\Delta}^T \mathbf{G}^T + \mathbf{G} \mathbf{\Delta} \mathbf{\Delta}^T \partial \mathbf{G}^T \\ &+ \partial \mathbf{G} \mathbf{\Sigma} \mathbf{\Sigma}^T \mathbf{G}^T + \mathbf{G} \mathbf{\Sigma} \mathbf{\Sigma}^T \partial \mathbf{G}^T. \end{aligned} \quad (74)$$

Recall from Equation 72 that the gradient of the covariance enters into the negative log-likelihood gradient through a quadratic form, $\mathbf{d}^T \partial \mathbf{C}^{-1} \mathbf{d}$, and through a product with a symmetric matrix and a subsequent trace via $\text{Tr}(\mathbf{C}^{-1} \partial \mathbf{C})$. Consequently, we may instead use

$$\partial \mathbf{C} = 2\partial \mathbf{G} \left(\mathbf{\Delta} \mathbf{\Delta}^T + \mathbf{\Sigma} \mathbf{\Sigma}^T \right) \mathbf{G}^T \quad (75)$$

when computing the gradient of the negative log-likelihood. Inserting the identity after the gradient of the gain matrix via $\mathbf{I} = \mathbf{G}^{-1} \mathbf{G}$ and simplifying with Equation 46, we may rewrite the above expression as

$$\partial \mathbf{C} = 2\partial \mathbf{G} \mathbf{G}^{-1} (\mathbf{C} - \mathbf{N}). \quad (76)$$

With the simplified expression for the covariance gradient, the gradient of the χ^2 term, $\partial \chi^2 = \mathbf{d}^T \partial \mathbf{C}^{-1} \mathbf{d}$, can be written as

$$\mathbf{d}^T \partial \mathbf{C}^{-1} \mathbf{d} = -2\mathbf{p}^T \partial \mathbf{G} \mathbf{q}, \quad (77)$$

where $\mathbf{p} \equiv \mathbf{C}^{-1} \mathbf{d}$ and $\mathbf{q} \equiv \mathbf{G}^{-1} (\mathbf{C} - \mathbf{N}) \mathbf{p}$. Expanding the model covariance with Equation 46 and simplifying, the vector \mathbf{q} can equivalently be written as $\mathbf{q} = (\mathbf{\Delta} \mathbf{\Delta}^T + \mathbf{\Sigma} \mathbf{\Sigma}^T) \mathbf{G}^T \mathbf{p}$. Since the gain matrix is block-diagonal with 2×2 blocks

$$\mathbf{G}_k = \begin{pmatrix} G_k^R & -G_k^I \\ G_k^I & G_k^R \end{pmatrix}, \quad (78)$$

the χ^2 gradient is just a sum over baselines,

$$\mathbf{d}^T \partial \mathbf{C}^{-1} \mathbf{d} = -2 \sum_k \mathbf{p}_k^T \partial \mathbf{G}_k \mathbf{q}_k, \quad (79)$$

where $\mathbf{p}_k^T = (p_k^R, p_k^I)$ and $\mathbf{q}_k^T = (q_k^R, q_k^I)$. Evaluating the quadratic form allows us to rewrite the χ^2 gradient as

$$\mathbf{d}^T \partial \mathbf{C}^{-1} \mathbf{d} = -2 \sum_k s_k \partial G_k^R + t_k \partial G_k^I, \quad (80)$$

where $s_k = p_k^R q_k^R + p_k^I q_k^I$ and $t_k = p_k^I q_k^R - p_k^R q_k^I$. The gradient of the χ^2 term may therefore be reduced to a single sum over baselines.

The trace term in Equation 72 may also be written as a sum over baselines. To see this, we first insert the simplified expression for the gradient of the covariance from Equation 76 into the trace term to obtain

$$\text{Tr}(\mathbf{C}^{-1} \partial \mathbf{C}) = 2\text{Tr}(\mathbf{C}^{-1} \partial \mathbf{G} \mathbf{G}^{-1} (\mathbf{C} - \mathbf{N})). \quad (81)$$

Applying the cyclic property of the trace and distributing the inverse covariance, we may rewrite the previous expression as

$$\text{Tr}(\mathbf{C}^{-1} \partial \mathbf{C}) = 2\text{Tr}(\partial \mathbf{G} \mathbf{G}^{-1} (\mathbf{I} - \mathbf{N} \mathbf{C}^{-1})). \quad (82)$$

Inserting the sparse representation of the inverse covariance (Equation 63), the trace term then becomes

$$\text{Tr}(\mathbf{C}^{-1} \partial \mathbf{C}) = 2\text{Tr}(\partial \mathbf{G} \mathbf{G}^{-1} \mathbf{N} (\bar{\mathbf{\Delta}} \bar{\mathbf{\Delta}}^T + \bar{\mathbf{\Sigma}} \bar{\mathbf{\Sigma}}^T)). \quad (83)$$

Since the gain matrix is block-diagonal and the noise matrix is diagonal, the trace is just a sum of traces of products of 2×2 matrices,

$$\text{Tr}(\mathbf{C}^{-1} \partial \mathbf{C}) = 2 \sum_k \text{Tr}(\partial \mathbf{G}_k \mathbf{G}_k^{-1} \mathbf{N}_k \bar{\mathbf{P}}_k), \quad (84)$$

where the matrix $\bar{\mathbf{P}}_k$ is defined as

$$\begin{aligned} \bar{\mathbf{P}}_k = & \sum_{\lambda} \begin{pmatrix} (\bar{\Delta}_{k\lambda}^R)^2 & \bar{\Delta}_{k\lambda}^R \bar{\Delta}_{k\lambda}^I \\ \bar{\Delta}_{k\lambda}^R \bar{\Delta}_{k\lambda}^I & (\bar{\Delta}_{k\lambda}^I)^2 \end{pmatrix} \\ & + \sum_j \begin{pmatrix} (\bar{\Sigma}_{kj}^R)^2 & \bar{\Sigma}_{kj}^R \bar{\Sigma}_{kj}^I \\ \bar{\Sigma}_{kj}^R \bar{\Sigma}_{kj}^I & (\bar{\Sigma}_{kj}^I)^2 \end{pmatrix}. \end{aligned} \quad (85)$$

Note that $\bar{\mathbf{P}}_k$ has the generic structure

$$\bar{\mathbf{P}}_k = \begin{pmatrix} a_k & b_k \\ b_k & c_k \end{pmatrix}, \quad (86)$$

whereas the matrix product $\partial \mathbf{G} \mathbf{G}^{-1}$ has the generic structure

$$\partial \mathbf{G}_k \mathbf{G}_k^{-1} = \begin{pmatrix} d_k & e_k \\ -e_k & d_k \end{pmatrix}. \quad (87)$$

Since $\mathbf{N}_k = \sigma_k^2 \mathbf{I}$, each trace in Equation 84 generically looks like

$$\text{Tr}(\partial \mathbf{G}_k \mathbf{G}_k^{-1} \mathbf{N}_k \bar{\mathbf{P}}_k) = \sigma_k^2 d_k (a_k + c_k). \quad (88)$$

Defining the ‘‘inverse power’’ \bar{P}_k as

$$\bar{P}_k = \sum_{\lambda} (\bar{\Delta}_{k\lambda}^R)^2 + (\bar{\Delta}_{k\lambda}^I)^2 + \sum_j (\bar{\Sigma}_{kj}^R)^2 + (\bar{\Sigma}_{kj}^I)^2, \quad (89)$$

and noting that $\mathbf{G}_k^{-1} = |G_k|^{-2} \mathbf{G}_k^T$, with $|G_k|^2 = (G_k^R)^2 + (G_k^I)^2$, the trace may be written as a sum over baselines

$$\text{Tr}(\mathbf{C}^{-1} \partial \mathbf{C}) = 2 \sum_k \frac{\sigma_k^2 \bar{P}_k}{|G_k|^2} \left(G_k^R \partial G_k^R + G_k^I \partial G_k^I \right). \quad (90)$$

In order to evaluate the χ^2 gradient (Equation 80) and the log-determinant gradient (Equation 90), we must compute the gradients with respect to the gain matrix elements G_k^R and G_k^I . Recall that the complex gain matrix elements take the form

$$G_k = g_{k_1} g_{k_2}^*, \quad (91)$$

where k_1, k_2 denote the antennas that form baseline k . The gain matrix elements G_k^R and G_k^I are therefore

$$G_k^R = g_{k_1}^R g_{k_2}^R + g_{k_1}^I g_{k_2}^I, \quad (92a)$$

$$G_k^I = g_{k_1}^I g_{k_2}^R - g_{k_1}^R g_{k_2}^I. \quad (92b)$$

Since the calibration parameters are the real and imaginary parts of the gains, we have four terms to compute, which are

$$\frac{\partial G_k^R}{\partial g_a^R} = g_{k_1}^R \delta_{ak_2} + g_{k_2}^R \delta_{ak_1}, \quad (93a)$$

$$\frac{\partial G_k^R}{\partial g_a^I} = g_{k_1}^I \delta_{ak_2} + g_{k_2}^I \delta_{ak_1}, \quad (93b)$$

$$\frac{\partial G_k^I}{\partial g_a^R} = g_{k_1}^I \delta_{ak_2} - g_{k_2}^I \delta_{ak_1}, \quad (93c)$$

$$\frac{\partial G_k^I}{\partial g_a^I} = g_{k_2}^R \delta_{ak_1} - g_{k_1}^R \delta_{ak_2}. \quad (93d)$$

Since a given baseline only contributes to the gradient for two antennas, we may efficiently accumulate the gradient by looping over baselines and using Equation 93a–Equation 93d to determine which components of the gradient each baseline contributes to.

In addition to the χ^2 and log-determinant gradients, we must also compute the gradient of the phase normalization term,

$$-\log \mathcal{L}_\phi = \frac{\left| \sum_a \phi_a \right|^2}{N_{\text{ant}}^2 \sigma_{\text{phs}}^2}. \quad (94)$$

Since the gain phases are related to the real and imaginary components of the gains through $\phi_a = \tan^{-1}(g_a^I/g_a^R)$, the gradient of the phase normalization term is

$$-\partial \log \mathcal{L}_\phi = 2 \frac{\sum_a \phi_a}{N_{\text{ant}}^2 \sigma_{\text{phs}}^2} \sum_a \frac{1}{1 + (g_a^I/g_a^R)^2} \partial (g_a^I/g_a^R). \quad (95)$$

Writing $|g_a|^2 = (g_a^R)^2 + (g_a^I)^2$, we may simplify this to

$$-\partial \log \mathcal{L}_\phi = 2 \frac{\sum_a \phi_a}{N_{\text{ant}}^2 \sigma_{\text{phs}}^2} \sum_a \frac{(g_a^R)^2}{|g_a|^2} \partial (g_a^I/g_a^R). \quad (96)$$

Noting that $\sin \phi_a = g_a^I/|g_a|$ and $\cos \phi_a = g_a^R/|g_a|$, the phase normalization gradient may therefore be written as

$$-\frac{\partial \log \mathcal{L}_\phi}{\partial g_b^R} = -2 \frac{\sum_a \phi_a}{N_{\text{ant}}^2 \sigma_{\text{phs}}^2} \frac{\sin \phi_b}{|g_b|}, \quad (97a)$$

$$-\frac{\partial \log \mathcal{L}_\phi}{\partial g_b^I} = 2 \frac{\sum_a \phi_a}{N_{\text{ant}}^2 \sigma_{\text{phs}}^2} \frac{\cos \phi_b}{|g_b|}. \quad (97b)$$

This completes the set of equations needed to analytically compute the gradient of the negative log-likelihood (Equation 72).

4.3. Performance

In this section, we briefly discuss the computational complexity of the algorithm reviewed in the previous section. In our analytic scaling calculations, we assume that the number of baselines N_{bl} greatly exceeds the number of sources N_{src} and the number of complex eigenmodes N_{eig} used to construct the source matrix Σ and the diffuse matrix Δ , respectively. Under this assumption, the rate limiting step in our implementation of the likelihood evaluation algorithm scales as $\mathcal{O}(N_{\text{bl}}(N_{\text{src}}^2 + N_{\text{eig}}^2))$. The rate limiting step in the gradient calculation also scales with the number of baselines, but with a different prefactor that is evidently larger than that of the likelihood evaluation, as seen in Figure 2.

In Figure 2, we show the average single-core execution time for various components of the CorrCal algorithm as a function of number of antennas. We carried out the performance test on a laptop using a single Intel i7-8565U processor with minimal background processes active. For each data point in Figure 2, we ran 10 trials and estimated the average walltime for inverting the covariance without computing the log-determinant, inverting the covariance while also accumulating the log-determinant, computing the negative log-likelihood, and computing the gradient of the negative log-likelihood. For the arrays with less than 100 antennas, we ran 1000 iterations per trial, and for the arrays with at least 100 antennas we reduced this to 100 iterations per trial. The variance in the estimated compute times is negligible for the majority of test cases—the only exceptions were the tests with a small number of antennas, where overheads dominated the runtime. We find that the compute times roughly scale with the number of baselines $N_{\text{bl}} \sim N_{\text{ant}}^2$ and that for an array with 1000 antennas the negative log-likelihood can be computed in about 0.125 s and the gradient can be computed in about 0.19 s when calibrating with a single source and single eigenmode. This performance was obtained without any major optimizations beyond carefully choosing the order of operations. Substantial improvements in performance may therefore be obtained by implementations that more efficiently manage data transfer or by transferring the calculations to a GPU-based implementation.

5. VALIDATION

In order to test CorrCal’s efficacy, we perform a variety of test calibration runs with simulated data. These tests are intended to assess how the quality of calibration solutions obtained with CorrCal are related to modeling errors. In Section 5.1, we discuss the results of tests investigating how point source modeling errors affect the

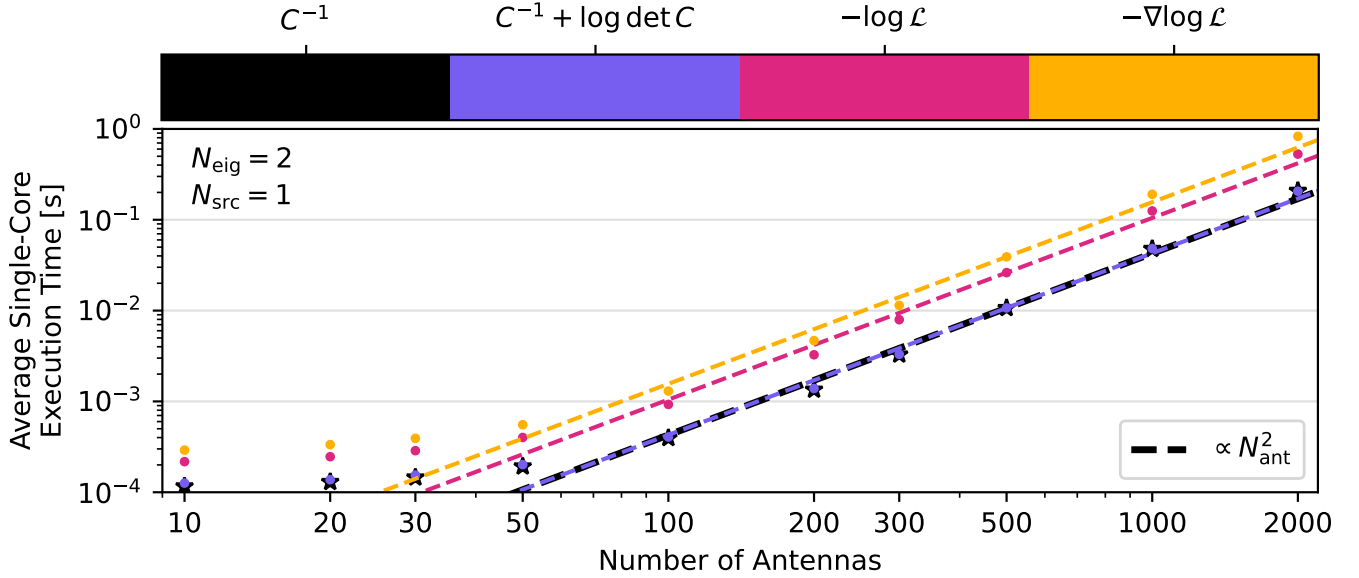


Figure 2. Results of a benchmark test for the single core execution time (using an Intel i7-8565U processor) of the most computationally intensive tasks in the CorrCal algorithm, shown as a function of array size: black shows the average time to invert the covariance; purple shows the time to invert the covariance and simultaneously accumulate the log-determinant; pink shows the total time for computing the negative log-likelihood; and yellow shows the total time to compute the gradient of the negative log-likelihood. For arrays with less than roughly 100 antennas, the computational cost is dominated by overheads. For larger arrays, the computational cost of all the tasks investigated here roughly scales with the square of the number of antennas, or linearly with the number of baselines. The dashed lines indicate execution times that scale with the square of the number of antennas, normalized to the measured execution time for a 500-element array.

quality of calibration solutions. In Section 5.2, we investigate how CorrCal performs when applied to data with known positional nonredundancy (i.e., when the antenna positions deviate slightly from a regular grid placement). In Section 5.3, we apply CorrCal to simulated data featuring a realistic sky model to assess whether non-Gaussianities in the diffuse sky signal produce significant calibration errors. In Section 5.4, we examine the complex interaction between the observed sky, the point sources used for calibration, and spatial phase gradients in the CorrCal gain solutions. For all of the simulations, we use an Airy disk for the antenna response (i.e., a diffraction-limited beam for a uniformly illuminated dish), since it strikes a balance between moderate realism and computational simplicity. We perform all of our simulations at an observed frequency of 150 MHz, since this is contained in the HERA observing band and minimizes the computational resources required to simulate visibilities for the diffuse sky component.⁷ In Figure 3, we provide a view of a typical simulated sky used for the tests described in Section 5.1 and Section 5.2. All of the visibility simulations were performed with the `matvis`

package (Kittiwisit et al. 2025) using the wrappers available in `hera_sim`.⁸

5.1. Sky Modeling Errors

For this set of tests, we ran an ensemble of simulations where each simulation features a different level of inaccuracy in modeling the array response to point sources. We parametrize the source model accuracy by the number of sources included in the calibration model and the average error on the model source flux densities. For a test with N_{cal} calibration sources and an average fractional flux error $0 < \sigma < 1$, we construct the source matrix by taking the N_{cal} sources with the brightest observed flux and computing the source vectors according to Equation 50 with $S_j^{\text{model}} = S_j^{\text{true}}(1 + \varepsilon)$, where $\varepsilon \sim \mathcal{N}(0, \sigma^2)$. The complete set of tests explores the outer product of the parameter options listed in Table 1. Generically, a greater number of sources and a lower average error on the source flux densities corresponds to a more accurate source model. For all of the tests in this section, we use a 19-element hexagonal array of antennas with a nearest-neighbor separation of 14.6 m and a dish diameter of 14 m.

⁷ At high frequencies, the short fringe spacings require extremely high resolution pixellizations of the sky to avoid aliasing issues.

⁸ https://github.com/HERA-Team/hera_sim

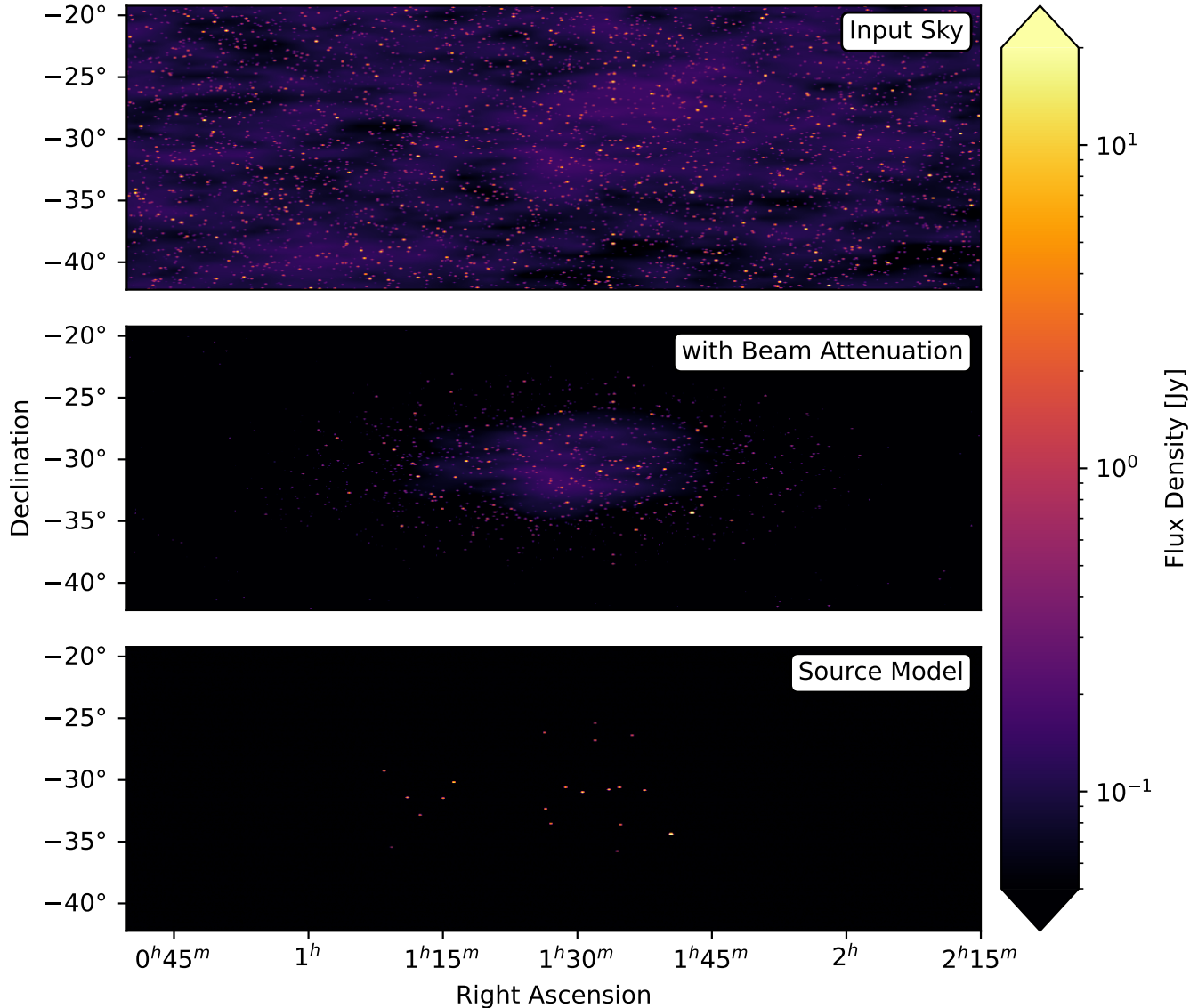


Figure 3. A representative view of the simulated sky, instrument response, and source model used in the tests in Section 5. The point sources shown in each panel have been smoothed with a $1'$ Gaussian kernel. The top panel shows the sky input to the visibility simulations for one of the “bright” fields with the diffuse component scaled down to increase the contrast with the point sources. The middle panel shows the same field, but with the primary beam attenuation applied. The bottom panel provides a representative view of the sources that would be included when modeling the source matrix Σ .

Table 1. Source Model Accuracy Test Parameters

Test Hyperparameter	Options
Average Flux Error [%]	(0, 1, 2, 5, 10, 20)
Number of Calibration Sources	(1, 5, 10, 20)

Importantly, practical applications of CorrCal will involve modeling a small number of sources on the sky,

since the rate limiting step in the likelihood evaluation scales with the square of the number of modeled sources (as discussed in Section 4.3). Because we will never calibrate with a complete sky model, we investigate how the quality of the calibration depends on the availability of bright point sources on the sky. To that end, we experiment with 10 realizations each of three different distributions of point sources on the sky. Each of these distributions uses the distribution of source fluxes reported in Franzen et al. (2019), but enforces different cutoffs in the maximum source flux at 150 MHz: the “quiet” field only includes sources up to 1 Jy; the

“average” field includes sources up to 100 Jy; and the “bright” field includes sources up to 100 Jy with an additional bright source whose flux ranges between 1 kJy and 10 kJy. For each of these fields, we only simulate sources in a $30^\circ \times 30^\circ$ patch of sky centered on zenith and enforce a common minimum flux cutoff of 100 mJy. This yields several thousand sources per simulation and should not produce qualitatively different results than simulating sources over the full sky since the simulated antenna response 30° away from zenith is suppressed by roughly a factor of 10^3 .

Each simulation also contains a diffuse sky component that is a realization of a Gaussian random field with an angular power spectrum $C_\ell \propto (1 + \ell)^{-2}$. To ensure that the diffuse sky component is non-negative, we add a monopole T_0 to the randomly generated diffuse map. We additionally rescale the diffuse component by a factor \mathcal{A} so that the maximum brightness in the generated map is 500 K, which is roughly comparable to the sky brightness away from the plane of the galaxy at 150 MHz. Accounting for the rescaling and monopole, the power spectrum of the simulated diffuse sky is

$$C_\ell^{\text{sim}} = \mathcal{A}^2 C_\ell^{\text{input}} (1 + 4\pi T_0^2 \delta_{\ell 0}). \quad (98)$$

We use this diffuse power spectrum, after converting it from temperature units to telescope units, when computing the diffuse matrix Δ .

The set of tests may be thought of as being split up into different “trials,” where each trial consists of 100 different calibration runs with different realizations of thermal noise. For each trial, we generate one set of per-antenna gains and one set of initial guesses for the gains that are fairly close to the true gains. The true gain phases are uniformly distributed on $[0, 2\pi)$, and the true gain amplitudes are normally distributed about unity with a standard deviation of 0.1. The phases of the initial guesses are normally distributed about the true phases with a standard deviation of 0.02 radians, and the ratios between the true amplitudes and the amplitudes of the initial guesses are normally distributed about unity with a standard deviation of 0.05. These parameters are summarized in Table 2. Since we would like to minimize the effect of thermal noise on the quality of the calibration solutions, we simulate radiometer noise such that the signal-to-noise ratio in the visibilities is roughly several hundred on average. Additionally, to minimize the errors from sample variance, we perform 10 trials for each choice of source modeling error and sky realization, providing us with a combined 720,000 calibration solution samples.

Table 2. Simulated Gain Parameters

Parameter	Distribution
True Gain Amplitude, g_a^{true}	$\mathcal{N}(1, 0.1^2)$
True Gain Phase, ϕ_a^{true}	Uniform($0, 2\pi$)
Initial Gain Amplitude Error, $\frac{g_a^{\text{init}}}{g_a^{\text{true}}}$	$\mathcal{N}(1, 0.05^2)$
Initial Gain Phase Error, $\phi_a^{\text{init}} - \phi_a^{\text{true}}$	$\mathcal{N}(0, 0.02^2)$

To assess the quality of the calibration solutions, we primarily rely on a chi-squared per degree of freedom statistic χ^2/DoF , as well as a p -value statistic, both of which are computed once per calibration run. We compute χ^2 via

$$\chi^2 = \sum_k \frac{|V_k^{\text{cal}} - V_k^{\text{true}}|^2}{\sigma_k^2}, \quad (99)$$

where σ_k^2 is the thermal noise variance in the visibility measured by baseline \mathbf{b}_k , V_k^{true} is the expected visibility, and V_k^{cal} is the calibrated visibility. Rather than use the gains directly from CorrCal to calibrate the simulated visibilities, we first apply an amplitude correction and phase slope correction to the gain solutions. In effect, we use the known true gains to perform absolute calibration through fitting for a phase slope and overall amplitude correction. The amplitude correction is necessary because CorrCal uses an incomplete model of point sources and a statistical description of diffuse emission, which results in a mismatch between the observed power and the measured power that manifests as an overall offset in the inferred gain amplitudes. The phase slope correction is necessary also because we are using an incomplete sky model, but the relation between model incompleteness and phase slope in the inferred gains is complex enough that we devote Section 5.4 to a more detailed discussion of the issue. Naturally, the presence of an amplitude offset and a phase slope means that practical applications of CorrCal ought to be supplemented by an absolute calibration step. Fortunately, however, the amplitude offset and phase slope tend to be small enough that the absolute calibration step will only very modestly change the calibration solutions. Science cases that do not share the extreme precision requirements of 21 cm cosmology may likely be able to use the CorrCal solutions as-is, but we advise that in such cases users perform tests to ensure that the expected amplitude offsets and phase slopes are indeed negligible for their science case.

If the best-fit gains from CorrCal are denoted \hat{g}_a , then the modified gains \hat{g}'_a are computed via

$$\hat{g}'_a = A \hat{g}_a \exp(i \nabla \Phi \cdot \mathbf{x}_a), \quad (100)$$

where \mathbf{x}_a is the position of antenna a in local coordinates. The amplitude correction A is computed as

$$A = \frac{\sum_a |g_a^{\text{true}}|}{\sum_a |\hat{g}_a|}, \quad (101)$$

while the phase slope $\nabla\Phi$ is obtained from a linear least-squares fit to the phase errors in the per-baseline gains, $\Delta\phi_k \equiv \arg(\hat{G}_k^* G_k^{\text{true}})$ by solving the system of equations

$$\Delta\phi_k = \mathbf{b}_k \cdot \nabla\Phi. \quad (102)$$

After performing the amplitude and phase slope correction, the calibrated visibilities are computed according to

$$V_k^{\text{cal}} = \frac{G_k^{\text{true}}}{G_k'} (V_k^{\text{true}} + n_k), \quad (103)$$

where $G_k' \equiv g_{k_1}' g_{k_2}'^*$ and n_k is the radiometer noise realization. Since we are performing an additional absolute calibration, the degrees of freedom in the calibrated visibilities are

$$\text{DoF} = 2N_{\text{bl}} - (2N_{\text{ant}} - 1 - 4), \quad (104)$$

since CorrCal used $2N_{\text{bl}}$ data points to solve for $2N_{\text{ant}}$ free parameters, which were further constrained by the amplitude and phase slope corrections. After computing χ^2 and the number of degrees of freedom, we may translate this into a p -value via

$$p = 1 - F_{\chi^2(\text{DoF})}(\chi^2), \quad (105)$$

where $F_{\chi^2(\text{DoF})}(\chi^2)$ is the cumulative probability of measuring χ^2 given a χ^2 distribution with DoF degrees of freedom. We then histogram the measured χ^2/DoF values and the corresponding p -values and compare the histograms against the distributions one would expect when errors in the calibrated visibilities are consistent with the thermal noise in the data.

The histogrammed χ^2/DoF and p values are shown in Figure 4. Rather than individually plot the histograms for each test we performed, we combine samples from all the tests and make a single histogram from the full population, as this allows us to obtain a more precise estimate of the error distribution. The decision to treat the entire suite of test results as a single population was based on an initial inspection of the histograms computed for each individual test, which revealed that the calibration errors seemed to be drawn from the same distribution. Because χ^2/DoF and p -value statistics are normalized against the noise amplitude, these statistics effectively brought the error distributions for each test to a common scale, which allowed us to perform a simple visual comparison of the histograms to assess

whether the errors for different tests were drawn from the same distribution. In addition to the χ^2/DoF and p -value histograms for the calibrated simulations, we show the histograms for “noise only” simulations where the “calibrated” visibilities entering into Equation 99 are $V_k^{\text{true}} + n_k$ as a reference—for this reference case, the visibilities differ from their expected value only by the injected thermal noise. Alongside the χ^2/DoF histograms, we plot the expected χ^2/DoF distributions, using $2N_{\text{bl}}$ degrees of freedom for the “noise only” case and Equation 104 for the simulations calibrated with CorrCal. The expected χ^2/DoF distribution is broader for the CorrCal output than for the “noise only” case, since there are fewer degrees of freedom in the data after calibration, as indicated by Equation 104. Said differently, because the constraints of calibration induce some degree of dependency between the residuals $V_k^{\text{cal}} - V_k^{\text{true}}$ that is absent from the “noise only” case (as those visibilities were not processed by CorrCal), and because the shape of a χ^2/DoF distribution is a function of the number of degrees of freedom, there is a difference between the expected χ^2/DoF distribution for the CorrCal residuals and the expected χ^2/DoF distribution for the “noise only” residuals. The stepped lines indicate the histograms taken over all samples, while the shaded regions indicate the range of histogram values when the histograms are computed separately for each test setting (i.e., each unique combination of number of sources, average flux error, and field type). We find excellent agreement with the expected χ^2/DoF distributions and excellent agreement with a uniform p -value distribution, which indicates that the residuals in the calibrated visibilities are consistent with the thermal noise injected into the simulations. We therefore conclude that, when the data are perfectly redundant, CorrCal is robust to errors in the source fluxes and the quality of the calibration solutions is fairly insensitive to the number of sources included in the model—there is no evidence of systematic calibration errors due to missing or incorrect flux in the source model, at least within the bounds of the scenarios investigated in this paper.

5.2. Nonredundancy Tests

To assess the performance of CorrCal in the presence of array nonredundancy, we perform a set of simulations inspired by those performed in Sievers (2017). For these tests, we use an 8×8 rectangular array of parabolic reflector antennas. The dish of each antenna has a diameter of 14 wavelengths, and nearest neighbors are separated by 20 wavelengths. We ran 100 simulations for each sky model used in Section 5.1 for a total of 3000 test simulations. In each simulation, we apply Gaus-

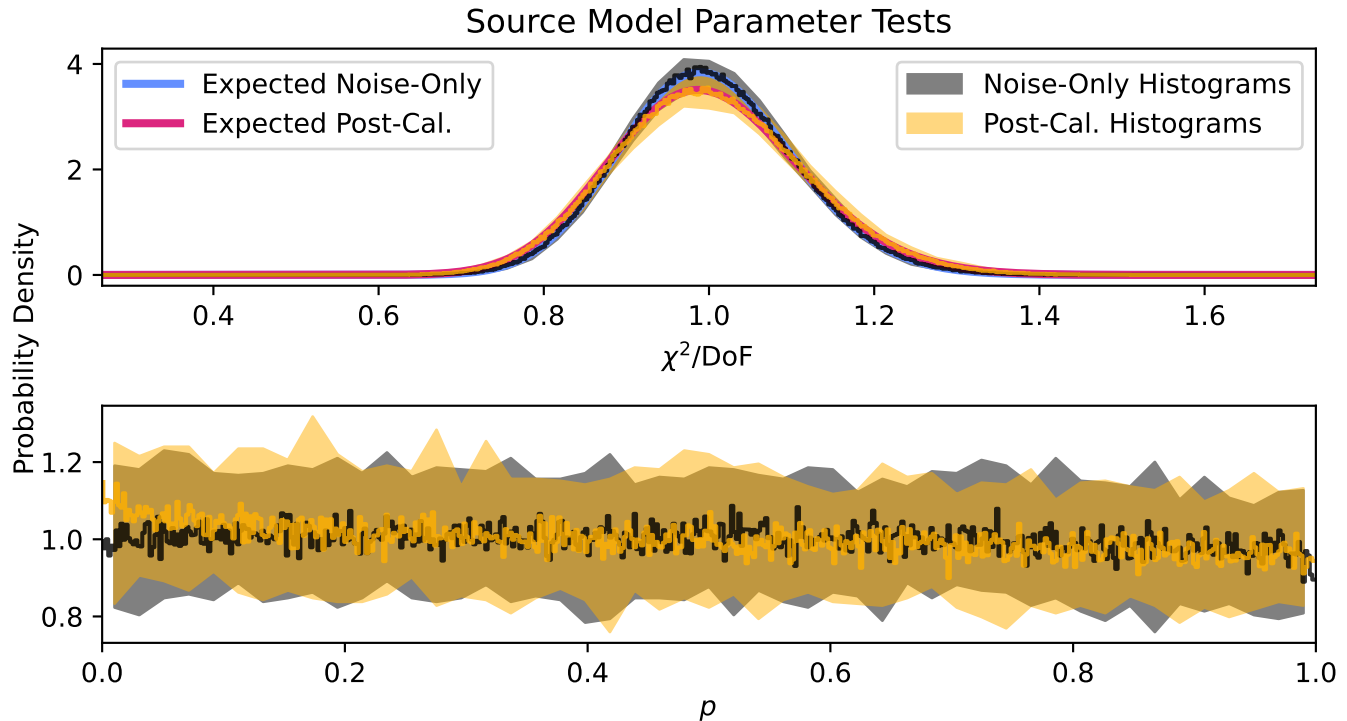


Figure 4. χ^2/DoF histograms (*top panel*) and p -value histograms (*bottom panel*) for the source model tests described in Section 5.1. The stepped lines indicate histograms computed using the full set of 720,000 samples, and the shaded regions indicate the range of histogram values obtained when histograms are computed over the 1,000 samples used per unique combination of source flux error, number of sources, and field type. The yellow lines and yellow shaded regions correspond to the histograms computed using the calibrated visibilities, while the black lines and black shaded regions correspond to the histograms computed for the “perfectly calibrated” visibilities. The thick solid lines in the top panel indicate the expected χ^2/DoF distributions when deviations from the true visibilities are consistent with the level of thermal noise injected into the simulations. The χ^2/DoF histograms are in excellent agreement with the expected distribution, and the p -value histograms are in excellent agreement with a uniform distribution, which suggests that there are no systematic calibration errors associated with missing flux or errors in the modeled source fluxes.

sian random perturbations to the antenna positions in the plane of the array with a standard deviation of 0.04 wavelengths (or roughly 0.003 dish diameters) in each direction. This is on the higher end of realistic positioning errors—for example, HERA dishes deviate from a regular grid at the scale of a few centimeters (so slightly less than 0.003 dish diameters), and CHORD dishes are expected to deviate from a regular grid at about the millimeter scale. We simulate per-antenna gains and initial guesses in the same fashion as described in Section 5.1, and add a small amount of radiometer noise to the visibilities (at roughly one fifth the level used in Section 5.1).

For each simulation, we perform calibration four different ways, each starting from the same initial guess at the per-antenna gains.

1. The first calibration run uses tools from the `hera_cal` package⁹ to perform redundant calibration. Since redundant calibration also requires a reasonable initial guess for the redundant visibilities, we provide the redundantly-averaged noiseless visibilities as an initial guess. This calibration run serves as our reference, as it is representative of the initial calibration step applied to arrays like HERA (Dillon et al. 2020).
2. The second calibration run uses CorrCal in a redundant calibration analog, where no point sources are modeled (i.e., $\Sigma_{kj} = 0$) and the diffuse matrix Δ is computed using the ideal antenna positions. Since the array is assumed to be perfectly redundant in this scenario, we only use a single complex eigenmode (or two real eigenmodes) for

⁹ https://github.com/HERA-Team/hera_cal/

this test. This is representative of what one might do when there are unknown positioning errors in the array and a lack of good calibration sources. In addition, this test serves as a crucial sanity check, as we should expect to obtain results very similar to those obtained by redundant calibration.

3. The third calibration run uses CorrCal without point source information but uses the exact antenna positions when computing the diffuse matrix. This scenario brings us closer to a realistic application of CorrCal, where we have surveyed the actual antenna positions but have not yet brought to bear information about bright sources on the sky.
4. The fourth calibration run uses the exact antenna positions to compute the diffuse matrix and includes the ten point sources that contribute the most to the observed flux in the source matrix Σ . This is representative of how one would run CorrCal as-is for a real experiment, leveraging information about array irregularities as well as about the sky.

For the last two calibration runs, we use the three complex eigenmodes (or six real modes) with the largest eigenvalues for each redundant block when constructing the diffuse matrix. Loosely speaking, the first eigenmode captures the redundant visibility for each group, while the next two modes capture the covariance structure related to the North-South and East-West antenna position perturbations. Eigenmodes beyond the first three have values that are suppressed by a factor of roughly 10^8 relative to the largest eigenmode and a factor of roughly 10^4 relative to the next two largest eigenmodes. Just as in Section 5.1, we apply an overall amplitude and phase slope correction to the gain solutions obtained from each of the four calibration runs.

In Figure 5, we show histograms of the normalized residuals in the calibrated data. We calibrate the data in the same way as in Equation 103, then compute the difference with the input data $V_k^{\text{true}} + n_k$ and normalize by the amplitude of the noiseless data $|V_k^{\text{true}}|$. On top of the histograms we plot four contours corresponding to the 1σ region for normalized noise fluctuations of varying signal-to-noise ratios. In addition to the four colored contours, we plot in black the contours that contain approximately 68% of the samples in each histogram. More precisely, suppose we define the random variable

$$\epsilon \equiv \frac{V + n}{|V|}, \quad (106)$$

where $n \sim \mathcal{N}(0, \sigma^2)$ and V is deterministic. The quantity ϵ is then a Gaussian random complex variable with mean $\exp(i\arg(V))$ and variance SNR^{-2} , where

$$\text{SNR} \equiv \frac{|V|}{\sigma}, \quad (107)$$

and the contours in Figure 5 would contain on average 68% of the samples of ϵ for various choices of signal-to-noise ratio SNR. In other words, the colored contours in Figure 5 indicate the 1σ regions for visibilities that deviate from their expected value only through thermal noise fluctuations with a given signal-to-noise ratio. One interpretation of Figure 5 is then that the inverse of the radius of the black contour indicates the signal-to-noise ratio at which thermal fluctuations will be comparable to calibration errors associated with array nonredundancy.

There is a clear hierarchy in the results shown in Figure 5. Redundant calibration and the redundant analog version of CorrCal perform comparably to one another and produce the greatest errors in the calibrated visibilities of the four methods tested. For these first two cases, the fractional errors are mostly contained to 1% or less, with a shallow peak near zero and a rapid decrease in probability density beyond the 1% level. Including exact antenna positions when modeling the diffuse matrix significantly reduces the calibration errors, as evidenced by the more compact error distribution (which instead falls off around the 0.5% level) and the sharper peak near zero.¹⁰ Including information about point sources and accurate antenna positions provides the best results: the corresponding error distribution shows the sharpest peak near zero and the probability density of the fractional errors sharply falls off beyond the 0.5% level.

The salient interpretation of the results shown in Figure 5 is that the calibration errors associated with nonredundancy in the data are unbiased and subdominant to thermal fluctuations in the visibilities at the typical single integration and single channel level. For many modern drift-scanning interferometers, the signal-to-noise ratio in the cross-correlations is typically not very high. For example, in the simulations run in Section 5.3, the radiometer noise associated with a 10 s integration and 100 kHz channel width produces a signal-to-noise ratio that is on average less than 10. We therefore conclude that modest levels of nonredundancy will not significantly impact the quality of calibration solutions

¹⁰ The radial spurs in the error distribution are a consequence of excluding information about bright sources—although not shown here, these features vanish when the error distribution is computed without the results from the fields containing a very bright point source.

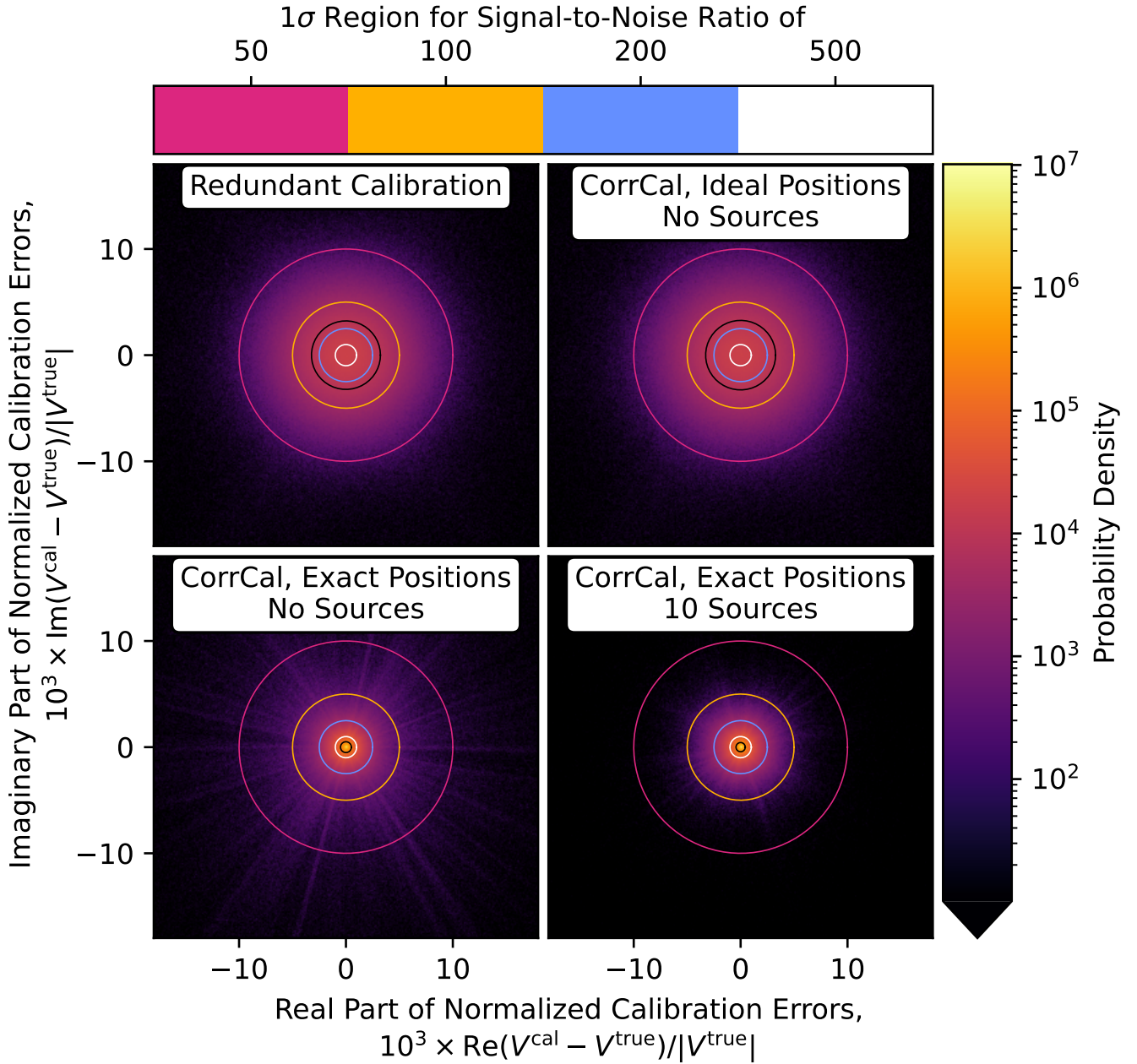


Figure 5. Histograms of the calibrated visibility residuals plotted in the complex plane for the four versions of calibration tested in Section 5.2. The calibration errors are computed relative to the true visibilities with noise and normalized by the amplitude of the true visibilities without noise. In the upper-left panel, we show the errors from running redundant calibration when the initial guess at the redundant visibilities is the redundant average of the true visibilities. In the upper-right panel, we show the errors from running CorrCal using a “redundant calibration analog” model covariance that excludes point sources and uses the ideal array layout for computing the diffuse matrix. Notably, the upper-right and upper-left panels are visually identical, indicating that applying CorrCal in “redundant calibration mode” reproduces the same errors as one gets when applying standard redundant calibration, as expected. In the bottom-left panel, we show the errors from running CorrCal where the model covariance excludes point sources and uses the exact antenna positions for computing the diffuse matrix. In the bottom-right panel, we show the errors from running CorrCal where the model covariance uses the exact antenna positions for computing both the source matrix and the diffuse matrix, where the ten sources that contribute the most to the observed flux are included in the source model. In each panel we also plot four contours corresponding to the 1 σ region for a complex Gaussian distribution with a given signal-to-noise ratio, as well as a black contour indicating the regions containing approximately 68% of the samples in the histograms.

Table 3. Summary of Errors in Gain Solutions

Calibration Type	$\sigma(g^{\text{true}} - \hat{g}')$	$\sigma(\phi^{\text{true}} - \hat{\phi}')$
Redundant Calibration	$2.5^{+0.8}_{-0.8} \times 10^{-3}$	$2.7^{+8.8}_{-1.5} \times 10^{-3}$
CorrCal, Ideal Positions	$2.6^{+0.8}_{-0.9} \times 10^{-3}$	$2.7^{+8.8}_{-1.5} \times 10^{-3}$
CorrCal, Exact Positions	$3.1^{+4.9}_{-1.5} \times 10^{-5}$	$1.9^{+7.8}_{-1.8} \times 10^{-3}$
CorrCal, with Sources	$2.4^{+1.3}_{-1.2} \times 10^{-5}$	$0.8^{+1.1}_{-0.6} \times 10^{-3}$

in realistic applications of CorrCal. We temper this conclusion, however, by noting that the calibration errors due to nonredundancy might not integrate down with time and may present as a systematic error in highly averaged data.

In addition to investigating the distribution of errors in the calibrated visibilities, we analyze the errors in the gain solutions themselves. To obtain a sense of how stable the gain solutions are across the array, we compute the standard deviation in the gain amplitude errors, $|g^{\text{true}}| - |\hat{g}'|$, as well as the standard deviation in the gain phase errors, $\phi^{\text{true}} - \phi' = \arg(g^{\text{true}} \hat{g}'^*)$, across the array. In Table 3, we provide a summary of our results by indicating the bounds containing 95% of the amplitude and phase error standard deviations. The results in Table 3 provide an alternate insight into the hierarchy displayed in Figure 5: as more information is added to the calibration model, there is less variance in the calibration errors.

5.3. Non-Gaussian Sky Test

As a final test, we ran CorrCal on simulated data using a realistic model of the sky when simulating visibilities. Importantly, this test explicitly breaks the assumption of Gaussianity in the diffuse emission on the sky, essentially bringing to bear an end-to-end test of the claim made in Section 2.1 and in Sievers (2017) that non-Gaussianity in the foregrounds would not affect the quality of the calibration solutions. We simulate data for a 61-element hexagonal array located at the HERA site at a local sidereal time of $2^h 0^m$ and a frequency of 151 MHz. Each antenna is 14 m in diameter with a diffraction-limited (i.e., Airy disk) beam and nearest neighbor antennas are separated by 14.6 m. The synthesized beam for this array has a full-width at half-maximum of about one degree. The point sources in the sky model are taken from the GLEAM catalog (Hurley-Walker et al. 2016) using the integrated flux densities at 151 MHz and including all sources above the horizon (roughly 161,000 sources in total) at the chosen observation time and telescope location. We additionally in-

clude the Global Sky Model (De Oliveira-Costa et al. 2008) interpolated to 151 MHz and downsampled to a resolution of roughly half a degree as the diffuse sky component. We simulate gains in the same manner as the previous sections but do not add any thermal noise to the simulated visibilities. For the source matrix, we include the top ten contributors to the observed flux, and for the diffuse matrix we use the angular power spectrum of the interpolated Global Sky Model.

In Figure 6 we show the errors in the amplitude and phase of the gain solutions. As in the previous sections, prior to computing the residuals we apply an overall amplitude correction and a phase slope correction to the calibration solution. The errors in the calibration solutions are small: amplitude errors typically occur at the $\lesssim 10^{-4}$ level and phase errors are typically around 10^{-7} rad, however the distribution of amplitude and phase errors may change depending on which part of the sky is overhead. While this is not an exhaustive test of how CorrCal performs with a realistic sky, these results suggest that calibration errors due to non-Gaussianities in the diffuse emission are negligible in applications with realistic noise levels. We therefore conclude that treating the diffuse emission on the sky as a Gaussian random field is valid for the purposes of calibration via CorrCal.

5.4. Phase Gradients

Recall from Section 4.3 that the rate-limiting step in the CorrCal algorithm scales as $\mathcal{O}(N_{\text{bl}}(N_{\text{src}}^2 + N_{\text{eig}}^2))$. Because the computational complexity scales with the square of the number of calibration sources, it is of practical interest that we calibrate with as few sources as possible, and we showed in Section 5.1 that CorrCal can obtain good calibration solutions with just a few calibration sources. One consequence of calibrating with an incomplete sky model, however, is the presence of a spatial phase gradient in the calibration solutions. More precisely, the best-fit gains \hat{g}_a differ from the true gains g_a^{true} through a phase factor that depends on the position of the antenna in the array \mathbf{x}_a via

$$\hat{g}_a = g_a^{\text{true}} e^{-i \nabla \Phi \cdot \mathbf{x}_a}, \quad (108)$$

where we refer to $\nabla \Phi^T = (\partial_x \Phi, \partial_y \Phi)$ as the phase gradient in the calibration solutions. In terms of the calibrated visibilities, this manifests as an effective pointing error, since

$$\frac{g_i^{\text{true}} (g_j^{\text{true}})^*}{\hat{g}_i \hat{g}_j^*} V_{ij} = \int A(\boldsymbol{\theta}) I(\boldsymbol{\theta}) e^{-i(2\pi\nu\boldsymbol{\theta}/c - \nabla\Phi) \cdot \mathbf{b}_{ij}} d\boldsymbol{\theta}. \quad (109)$$

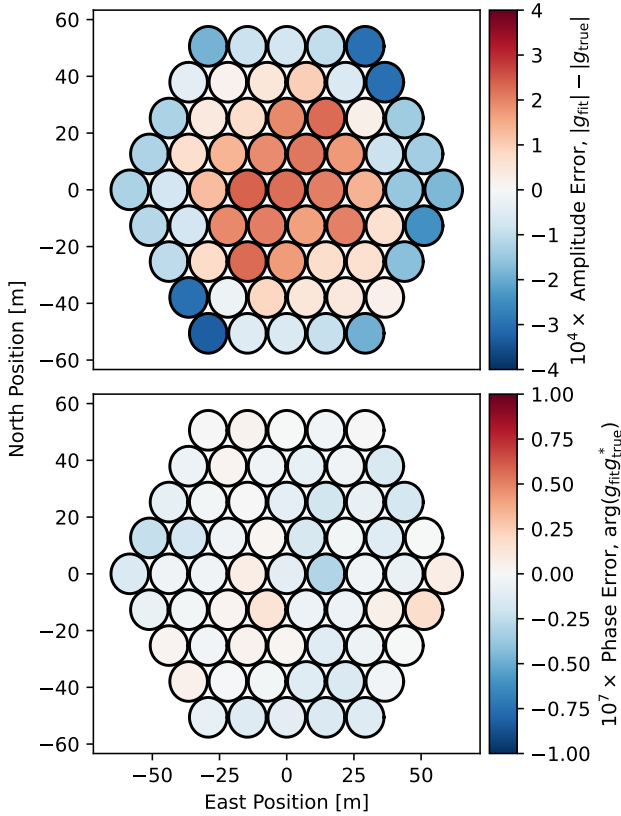


Figure 6. Errors in the gain amplitudes (*top panel*) and the gain phases (*bottom panel*) obtained for noiseless simulations using a realistic sky, as described in Section 5.3. The gain errors are computed after applying an overall amplitude and phase slope correction to the calibration solutions. Errors in the gain amplitudes and gain phases are small, which suggests that non-Gaussianities in the diffuse emission do not strongly impact the quality of the gain solutions.

Calibrating the data using gains that contain a phase gradient therefore shifts the inferred sky by an amount

$$\Delta\theta = \frac{\lambda}{2\pi} \nabla\phi, \quad (110)$$

where $\lambda = c/\nu$ is the observed wavelength. In redundant calibration, the phase gradient is a genuine degeneracy in the calibration solutions (Liu et al. 2010; Dillon et al. 2018) that must be resolved with an additional absolute calibration step. In CorrCal, the inclusion of bright point sources breaks this degeneracy; however, this does not mean that the CorrCal solutions are free of a phase gradient, since the missing flux from the source model is absorbed into the calibration solutions as a preferred phase gradient, as demonstrated in Figure 7.

Figure 7 summarizes the results of a set of tests performed to demonstrate the behavior of the phase gradient in CorrCal solutions. These tests were designed to demonstrate that the phase gradient is a function

of both the flux on the sky and the sources used for calibration, and also show that the phase gradient becomes unconstrained when there is not a bright source overhead to serve as a reliable calibrator. With this in mind, we simulated visibilities for three different fields, which we visualize as maps made from the data in the bottom panels of Figure 7. In two of the fields, there are bright sources very close to zenith, while for the third field there are no bright sources overhead. For each of these three fields, we generated 100 independent samples of radiometer noise with a similar signal-to-noise ratio as we used for the tests in Section 5.1, providing us with 300 sets of visibilities to calibrate. We used a single set of per-antenna gains across all the calibration runs as the true gains that were applied to the data, and randomly generated 10 different sets of initial guesses of the gains using the procedure summarized in Table 2. For each realization of noise, initial guess, and field, we ran calibration with two different covariance models: one covariance model used the ten brightest observed sources, while the other used the brightest observed source. After obtaining the calibration solutions, we performed a linear least-squares fit to determine the phase gradients by comparing the recovered gain phases against the true gain phases.

The effective pointing errors associated with the recovered phase gradients are plotted in the top panel of Figure 7. For the two fields that contain bright sources, the phase gradients cluster around particular values of $\Delta\theta$ that differ between fields and between covariance models. For the field without bright sources, the phase gradients are scattered in 10 groups that correspond to the 10 different initial guesses for the gains—for this field, the calibration solutions settle into some local minimum that is determined by the initial guess. Evidently, in the absence of bright calibrator sources, the phase gradient is unconstrained by CorrCal. This should be expected, since in the absence of bright sources CorrCal effectively operates as a generalized version of redundant calibration. In the version of CorrCal investigated in this paper, where different frequency channels and different integrations are calibrated independently, Figure 7 indicates that a modest phase gradient calibration is required for precision cosmology applications. In a more generalized application, however, it seems plausible that leveraging known covariances in time and frequency to perform a joint fit across multiple times or frequencies could provide enough additional constraining power to produce calibration solutions without a phase gradient.

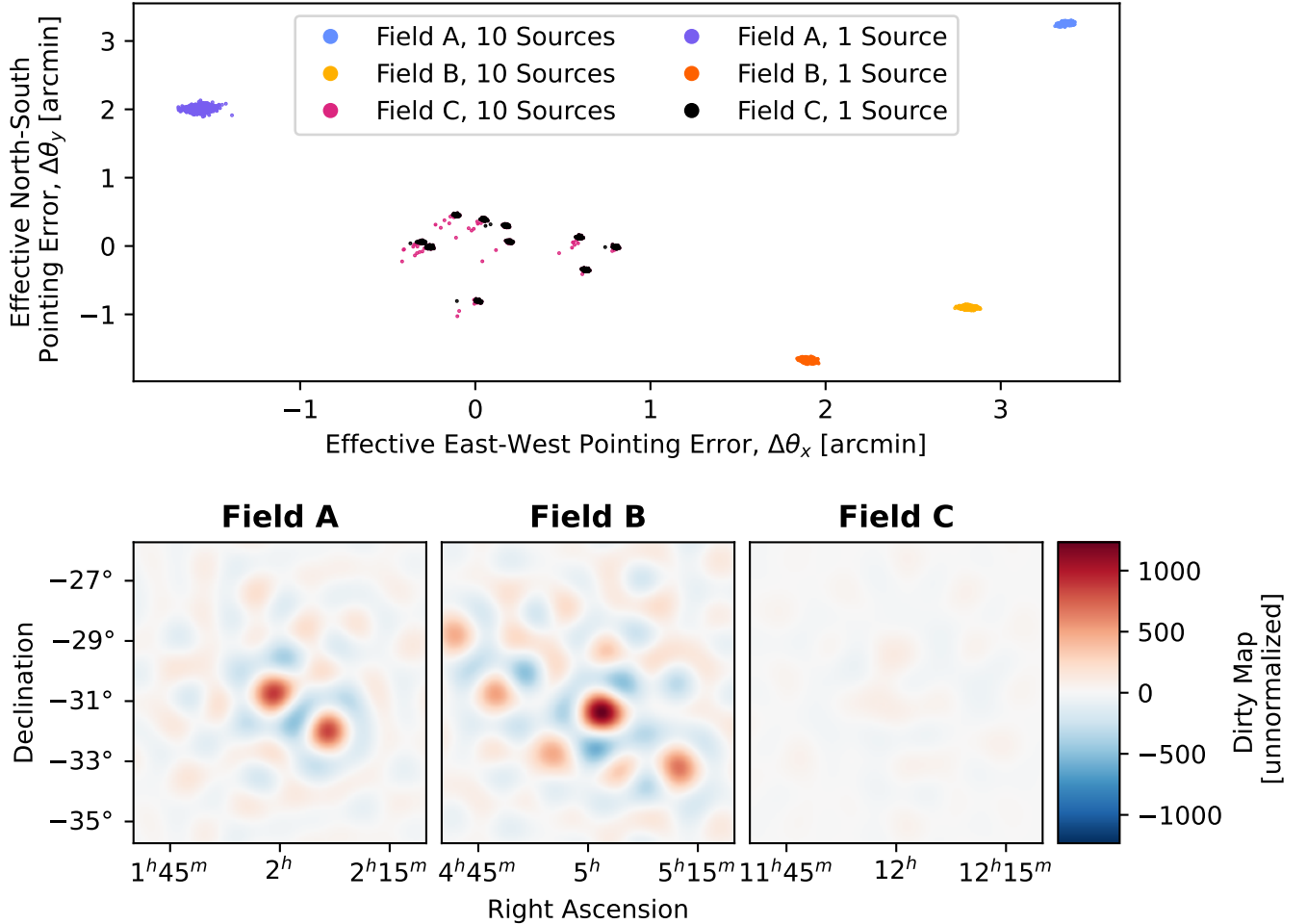


Figure 7. Demonstration that CorrCal constrains the phase gradient when there are bright point sources overhead. The bottom panels show the sky, as seen by the array (i.e., imaged by the array, but unnormalized), for three different fields used in the test. Field A (bottom left) and Field B (bottom middle) both contain bright point sources that provide a tight constraint on the gain phases. Field C (bottom right), however, does not contain any bright sources overhead. The top panel shows the phase gradient in the calibration solutions, converted to an effective pointing error, obtained with one calibration source and with ten calibration sources for each field across 100 independent noise realizations and 10 different initial guesses of the gains. For Field A and Field B, the phase gradients converge to values that depend on the number of calibration sources used. For Field C, the phase gradient is unconstrained, evidenced by the presence of multiple clusters of solutions, each of which correspond to a different initial guess of the gains.

6. CONCLUSION

In this paper, we provided an overview of the formalism supporting CorrCal, as well as its implementation, and presented the results of a set of tests designed to assess the accuracy of CorrCal in the presence of various modeling errors. We showed that, under an appropriate set of assumptions, the covariance between visibilities takes on a sparse form which may be leveraged to efficiently perform a covariance-based calibration of radio interferometric data. We found that CorrCal can obtain accurate calibration solutions by relying only on a handful of point sources, a model of the primary beam, and the power spectrum of the diffuse emission on the

sky. Moreover, the accuracy of the calibration solutions is relatively insensitive to missing or inaccurate source flux densities and positional nonredundancy in the array layout. A limited test with a realistic sky model also revealed that non-Gaussianities in the diffuse emission do not strongly affect the quality of the calibration solutions obtained with CorrCal. These tests collectively provide strong foundational support for CorrCal’s ability to obtain high quality calibration solutions in the presence of various modeling errors and array imperfections. Given the demonstrated success of CorrCal in our suite of validation tests, we are enthusiastic about future developments to CorrCal and forthcoming re-

sults of CorrCal applied to data from current and next-generation experiments, such as HERA and CHORD.

ACKNOWLEDGEMENTS

The authors thank Miguel Morales, Michael Wilensky, Kendrick Smith, Leon Koopmans, and Ruby Byrne for insightful conversations and helpful feedback. A.L. acknowledges support from an NSERC Discovery Grant, an Alliance International Grant, and the William Dawson Scholarship at McGill. R.P. acknowledges support from the Faculty of Arts & Science at the University of Toronto and the Dunlap Institute. The Dunlap Institute is funded through an endowment established by

the David Dunlap family and the University of Toronto. This work was funded in part by the Canada 150 Research Chairs Program. Research at Perimeter Institute is supported in part by the Government of Canada through the Department of Innovation, Science and Economic Development Canada and by the Province of Ontario through the Ministry of Colleges and Universities.

Software: `numpy` (Harris et al. 2020), `scipy` (Virtanen et al. 2020), `matplotlib` (Hunter 2007), `astropy` (Astropy Collaboration et al. 2022), `pyuvdata` (Hazelton et al. 2017)

REFERENCES

- Astropy Collaboration, Price-Whelan, A. M., Lim, P. L., et al. 2022, *The Astrophysical Journal*, 935, 167, doi: [10.3847/1538-4357/ac7c74](https://doi.org/10.3847/1538-4357/ac7c74)
- Barry, N., Hazelton, B., Sullivan, I., Morales, M. F., & Pober, J. C. 2016, *Monthly Notices of the Royal Astronomical Society*, 461, 3135, doi: [10.1093/mnras/stw1380](https://doi.org/10.1093/mnras/stw1380)
- Berkhout, L. M., Jacobs, D. C., Abdurashidova, Z., et al. 2024, *Publications of the Astronomical Society of the Pacific*, 136, 045002, doi: [10.1088/1538-3873/ad3122](https://doi.org/10.1088/1538-3873/ad3122)
- Byrne, R. 2023, *The Astrophysical Journal*, 943, 117, doi: [10.3847/1538-4357/acac95](https://doi.org/10.3847/1538-4357/acac95)
- Byrne, R., Morales, M. F., Hazelton, B. J., & Wilensky, M. 2021, *Monthly Notices of the Royal Astronomical Society*, 503, 2457, doi: [10.1093/mnras/stab647](https://doi.org/10.1093/mnras/stab647)
- Byrne, R., Morales, M. F., Hazelton, B., et al. 2019, *The Astrophysical Journal*, 875, 70, doi: [10.3847/1538-4357/ab107d](https://doi.org/10.3847/1538-4357/ab107d)
- CHIME Collaboration, Amiri, M., Bandura, K., et al. 2022, *The Astrophysical Journal Supplement Series*, 261, 29, doi: [10.3847/1538-4365/ac6fd9](https://doi.org/10.3847/1538-4365/ac6fd9)
- Cox, T. A., Parsons, A. R., Dillon, J. S., Ewall-Wice, A., & Pascua, R. 2024, *Monthly Notices of the Royal Astronomical Society*, 532, 3375, doi: [10.1093/mnras/stae1612](https://doi.org/10.1093/mnras/stae1612)
- Crichton, D., Aich, M., Amara, A., et al. 2022, *Journal of Astronomical Telescopes, Instruments, and Systems*, 8, 011019, doi: [10.1117/1.JATIS.8.1.011019](https://doi.org/10.1117/1.JATIS.8.1.011019)
- De Oliveira-Costa, A., Tegmark, M., Gaensler, B. M., et al. 2008, *Monthly Notices of the Royal Astronomical Society*, 388, 247, doi: [10.1111/j.1365-2966.2008.13376.x](https://doi.org/10.1111/j.1365-2966.2008.13376.x)
- DeBoer, D. R., Parsons, A. R., Aguirre, J. E., et al. 2017, *Publications of the Astronomical Society of the Pacific*, 129, 045001, doi: [10.1088/1538-3873/129/974/045001](https://doi.org/10.1088/1538-3873/129/974/045001)
- Dillon, J. S., Kohn, S. A., Parsons, A. R., et al. 2018, *Monthly Notices of the Royal Astronomical Society*, 477, 5670, doi: [10.1093/mnras/sty1060](https://doi.org/10.1093/mnras/sty1060)
- Dillon, J. S., Lee, M., Ali, Z. S., et al. 2020, *Monthly Notices of the Royal Astronomical Society*, 499, 5840, doi: [10.1093/mnras/staa3001](https://doi.org/10.1093/mnras/staa3001)
- Ewall-Wice, A., Dillon, J. S., Gehlot, B., et al. 2022, *The Astrophysical Journal*, 938, 151, doi: [10.3847/1538-4357/ac87b3](https://doi.org/10.3847/1538-4357/ac87b3)
- Franzen, T. M. O., Vernstrom, T., Jackson, C. A., et al. 2019, *Publications of the Astronomical Society of Australia*, 36, e004, doi: [10.1017/pasa.2018.52](https://doi.org/10.1017/pasa.2018.52)
- Harris, C. R., Millman, K. J., van der Walt, S. J., et al. 2020, *Nature*, 585, 357, doi: [10.1038/s41586-020-2649-2](https://doi.org/10.1038/s41586-020-2649-2)
- Hazelton, B. J., Jacobs, D. C., Pober, J. C., & Beardsley, A. P. 2017, *Journal of Open Source Software*, 2, 140, doi: [10.21105/joss.00140](https://doi.org/10.21105/joss.00140)
- HERA Collaboration, Abdurashidova, Z., Aguirre, J. E., et al. 2022, *The Astrophysical Journal*, 925, 221, doi: [10.3847/1538-4357/ac1c78](https://doi.org/10.3847/1538-4357/ac1c78)
- Hunter, J. D. 2007, *Computing in Science & Engineering*, 9, 90, doi: [10.1109/MCSE.2007.55](https://doi.org/10.1109/MCSE.2007.55)
- Hurley-Walker, N., Callingham, J. R., Hancock, P. J., et al. 2016, *Monthly Notices of the Royal Astronomical Society*, 464, 1146, doi: [10.1093/mnras/stw2337](https://doi.org/10.1093/mnras/stw2337)
- Joseph, R. C., Trott, C. M., & Wayth, R. B. 2018, *AJ*, 156, 285, doi: [10.3847/1538-3881/aaec0b](https://doi.org/10.3847/1538-3881/aaec0b)
- Kern, N. S., Dillon, J. S., Parsons, A. R., et al. 2020, *The Astrophysical Journal*, 890, 122, doi: [10.3847/1538-4357/ab67bc](https://doi.org/10.3847/1538-4357/ab67bc)
- Kittiwisit, P., Murray, S. G., Garsden, H., et al. 2025, *RAS Techniques and Instruments*, 4, rzaaf001, doi: [10.1093/rasti/rzaf001](https://doi.org/10.1093/rasti/rzaf001)
- Li, W., Pober, J. C., Hazelton, B. J., et al. 2018, *ApJ*, 863, 170, doi: [10.3847/1538-4357/aad3c3](https://doi.org/10.3847/1538-4357/aad3c3)

- Liu, A., & Shaw, J. R. 2020, Publications of the Astronomical Society of the Pacific, 132, 062001, doi: [10.1088/1538-3873/ab5bfd](https://doi.org/10.1088/1538-3873/ab5bfd)
- Liu, A., Tegmark, M., Morrison, S., Lutomirski, A., & Zaldarriaga, M. 2010, Monthly Notices of the Royal Astronomical Society, 408, 1029, doi: [10.1111/j.1365-2966.2010.17174.x](https://doi.org/10.1111/j.1365-2966.2010.17174.x)
- Myers, S. T., Contaldi, C. R., Bond, J. R., et al. 2003, The Astrophysical Journal, 591, 575, doi: [10.1086/375509](https://doi.org/10.1086/375509)
- Newburgh, L. B., Bandura, K., Bucher, M. A., et al. 2016, in Ground-based and Airborne Telescopes VI, ed. H. J. Hall, R. Gilmozzi, & H. K. Marshall, Vol. 9906, International Society for Optics and Photonics (SPIE), 99065X, doi: [10.1117/12.2234286](https://doi.org/10.1117/12.2234286)
- Orosz, N., Dillon, J. S., Ewall-Wice, A., Parsons, A. R., & Thyagarajan, N. 2019, Monthly Notices of the Royal Astronomical Society, 487, 537, doi: [10.1093/mnras/stz1287](https://doi.org/10.1093/mnras/stz1287)
- Sievers, J. L. 2017, Calibration of Quasi-Redundant Interferometers. <https://arxiv.org/abs/1701.01860>
- Sims, P. H., Pober, J. C., & Sievers, J. L. 2022a, Monthly Notices of the Royal Astronomical Society, 517, 910, doi: [10.1093/mnras/stac1861](https://doi.org/10.1093/mnras/stac1861)
- . 2022b, Monthly Notices of the Royal Astronomical Society, 517, 935, doi: [10.1093/mnras/stac1749](https://doi.org/10.1093/mnras/stac1749)
- Tan, J., Liu, A., Kern, N. S., et al. 2021, The Astrophysical Journal Supplement Series, 255, 26, doi: [10.3847/1538-4365/ac0533](https://doi.org/10.3847/1538-4365/ac0533)
- Vanderlinde, K., Liu, A., Gaensler, B., et al. 2020, The Canadian Hydrogen Observatory and Radio-transient Detector (CHORD), Zenodo, doi: [10.5281/zenodo.3765414](https://doi.org/10.5281/zenodo.3765414)
- Virtanen, P., Gommers, R., Oliphant, T. E., et al. 2020, Nature Methods, 17, 261, doi: [10.1038/s41592-019-0686-2](https://doi.org/10.1038/s41592-019-0686-2)
- Yatawatta, S., Zaroubi, S., de Bruyn, G., Koopmans, L., & Noordam, J. 2009, IEEE, Piscataway, NJ, 150

APPENDIX

A. REDUNDANT CALIBRATION LIMIT

In this appendix, we show how an appropriate choice of parameters for the model covariance results in the CorrCal chi-squared, χ_C^2 , converging to the redundant calibration chi-squared, χ_R^2 , evaluated at the best-fit visibility solutions. The redundant calibration chi-squared may be written as

$$\chi_R^2 = \sum_r \sum_{k \in r} \frac{|d_k - G_k V_r|^2}{\sigma_k^2}, \quad (\text{A1})$$

where V_r is the model visibility for redundant group r , $\sum_{k \in r}$ indicates a sum over all baselines within redundant group r , d_k is the visibility data for baseline \mathbf{b}_k , σ_k^2 is the noise variance, and $G_k \equiv g_{k_1} g_{k_2}^*$ is the product of the complex per-antenna gains. The gradient of χ_R^2 with respect to the model visibilities V_r may be written as

$$\frac{\partial \chi_R^2}{\partial V_r} = - \sum_{k \in r} \frac{(G_k d_k^* - |G_k|^2 V_r^*)}{\sigma_k^2}, \quad (\text{A2})$$

so the model visibilities at the minimum χ_R^2 are related to the gains via

$$\hat{V}_r = \frac{\sum_{k \in r} G_k^* d_k / \sigma_k^2}{\sum_{k \in r} |G_k|^2 / \sigma_k^2}. \quad (\text{A3})$$

If we define the parameters $\gamma_r \equiv \sum_{k \in r} G_k^* d_k / \sigma_k^2$ and $\beta_r \equiv \sum_{k \in r} |G_k|^2 / \sigma_k^2$, then the best-fit model visibilities are just $\hat{V}_r = \gamma_r / \beta_r$. Inserting the best-fit model visibilities into Equation A1, we get

$$\chi_R^2 \Big|_{V_r = \hat{V}_r} = \sum_r \sum_{k \in r} \frac{|d_k - G_k \gamma_r / \beta_r|^2}{\sigma_k^2}, \quad (\text{A4})$$

$$(\text{A5})$$

which may be simplified as

$$\chi_R^2 \Big|_{V_r = \hat{V}_r} = \sum_k \frac{|d_k|^2}{\sigma_k^2} - \sum_r \frac{|\gamma_r|^2}{\beta_r}. \quad (\text{A6})$$

This is exactly equal to the CorrCal chi-squared in a particular limiting case, as we will show below.

In the case that no point sources are included in the model covariance, the data may be treated as circularly symmetric Gaussian random variables, and we may therefore use the complex-valued data and complex-valued model covariance so that

$$\chi_C^2 = \mathbf{d}^\dagger \mathbf{C}^{-1} \mathbf{d}, \quad (\text{A7})$$

where $\mathbf{d}^T = (d_1, \dots, d_N)$, and $\mathbf{C} = \mathbf{N} + \mathbf{G} \mathbf{\Delta} \mathbf{\Delta}^\dagger \mathbf{G}^\dagger$. Note that in this representation, the noise matrix \mathbf{N} and gain matrix \mathbf{G} are both diagonal. For the diffuse matrix, we use a block-diagonal parametrization with

$$\mathbf{\Delta} = \text{diag}(\dots, V_r \mathbf{1}, \dots), \quad (\text{A8})$$

where $\mathbf{1}$ is a vector of ones and V_r is the model visibility for redundant group r . In order to compute χ_C^2 , we will need to manually compute \mathbf{C}^{-1} , which we can do by applying the Woodbury identity so that

$$\mathbf{C}^{-1} = \mathbf{N}^{-1} - \mathbf{N}^{-1} \mathbf{G} \mathbf{\Delta} (\mathbf{I} + \mathbf{\Delta}^\dagger \mathbf{G}^\dagger \mathbf{N}^{-1} \mathbf{G} \mathbf{\Delta})^{-1} \mathbf{\Delta}^\dagger \mathbf{G}^\dagger \mathbf{N}^{-1}, \quad (\text{A9})$$

where \mathbf{I} is the identity matrix. Since $\mathbf{\Delta}$ is block-diagonal, and both \mathbf{G} and \mathbf{N} are diagonal, the small inverse in the above expression may be written as

$$\left[(\mathbf{I} + \mathbf{\Delta}^\dagger \mathbf{G}^\dagger \mathbf{N}^{-1} \mathbf{G} \mathbf{\Delta})^{-1} \right]_{rr'} = \frac{\delta_{rr'}}{1 + |V_r|^2 \sum_{k \in r} |G_k|^2 / \sigma_k^2}, \quad (\text{A10})$$

which may be simplified as

$$\left[(\mathbf{I} + \mathbf{\Delta}^\dagger \mathbf{G}^\dagger \mathbf{N}^{-1} \mathbf{G} \mathbf{\Delta})^{-1} \right]_{rr'} = \delta_{rr'} (1 + |V_r|^2 \beta_r)^{-1}. \quad (\text{A11})$$

The final ingredient to compute the CorrCal χ^2 in this limit is the vector $\mathbf{\Delta}^\dagger \mathbf{G}^\dagger \mathbf{N}^{-1} \mathbf{d}$. Since \mathbf{G} and \mathbf{N} are diagonal, $\mathbf{G}^\dagger \mathbf{N}^{-1} \mathbf{d}$ just scales each component of \mathbf{d} , and contracting the result with $\mathbf{\Delta}^\dagger$ results in sums over redundant groups so that

$$\left(\mathbf{\Delta}^\dagger \mathbf{G}^\dagger \mathbf{N}^{-1} \mathbf{d} \right)_r = V_r^* \sum_{k \in r} \frac{G_k^* d_k}{\sigma_k^2}, \quad (\text{A12})$$

which we may simplify as

$$\left(\mathbf{\Delta}^\dagger \mathbf{G}^\dagger \mathbf{N}^{-1} \mathbf{d} \right)_r = V_r^* \gamma_r. \quad (\text{A13})$$

Taking all these results together, the CorrCal chi-squared can be written as

$$\chi_C^2 = \sum_k \frac{|d_k|^2}{\sigma_k^2} - \sum_r \frac{|V_r|^2 |\gamma_r|^2}{1 + |V_r|^2 \beta_r}. \quad (\text{A14})$$

If we take the limit $|V_r| \rightarrow \infty$, we get

$$\lim_{|V_r| \rightarrow \infty} \chi_C^2 = \sum_k \frac{|d_k|^2}{\sigma_k^2} - \sum_r \frac{|\gamma_r|^2}{\beta_r} = \chi_R^2 \Big|_{V_r = \hat{V}_r}. \quad (\text{A15})$$

CorrCal therefore reduces to redundant calibration when we do not include any source modeling, exclude the determinant normalization in the likelihood, and take the limit that the redundant visibilities are large relative to the noise amplitude.